Oxygen Reduction Reaction

DOI: 10.1002/anie.201207186

Tuning Nanoparticle Catalysis for the Oxygen Reduction Reaction

*Shaojun Guo, Sen Zhang, and Shouheng Sun**

Keywords:
alloys · core–shell nanoparticles · fuel cells · oxygen reduction reaction · platinum

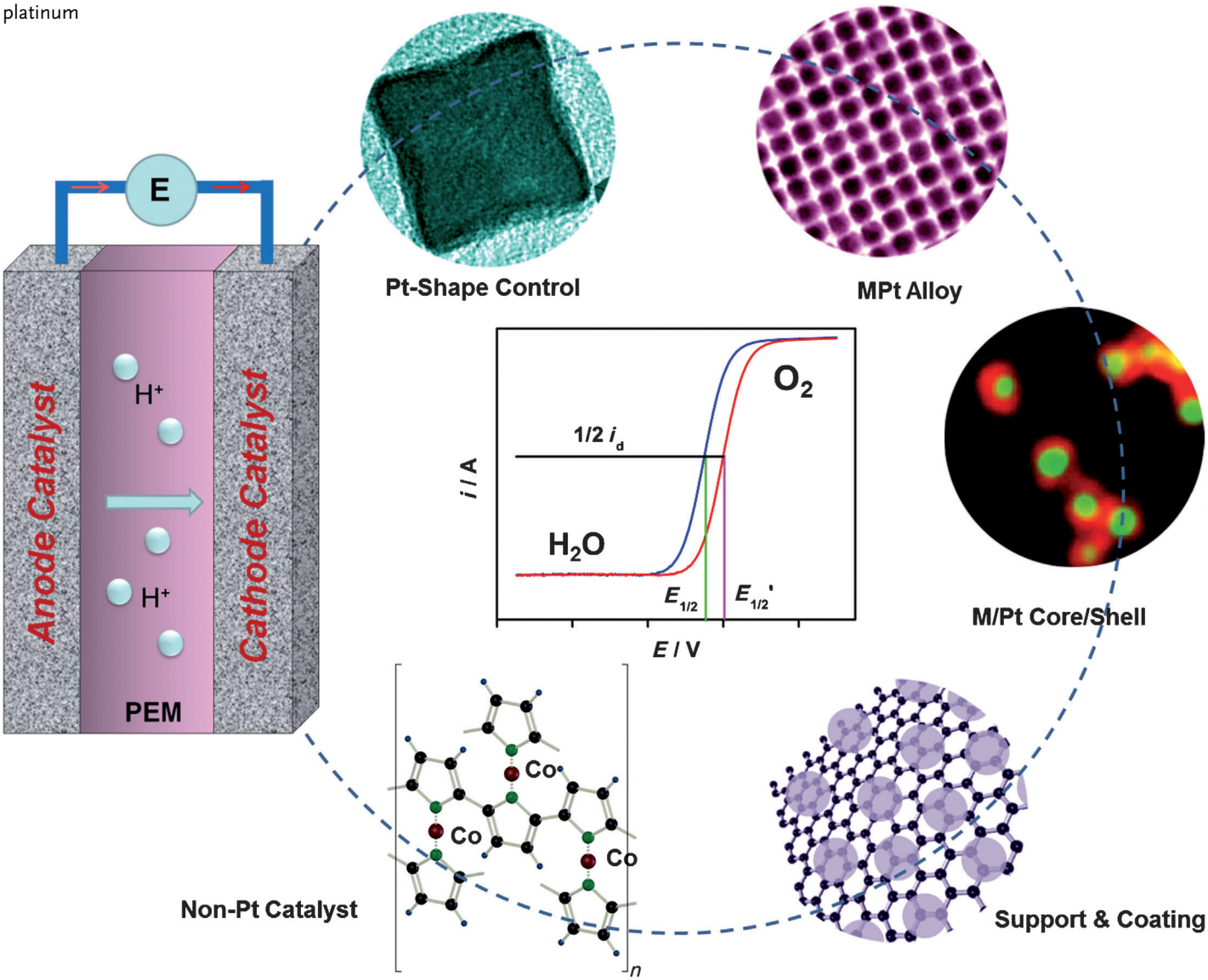

Advances in chemical syntheses have led to the formation of various kinds of nanoparticles (NPs) with more rational control of size, shape, composition, structure and catalysis. This review highlights recent efforts in the development of Pt and non-Pt based NPs into advanced nanocatalysts for efficient oxygen reduction reaction (ORR) under fuel-cell reaction conditions. It first outlines the shape controlled synthesis of Pt NPs and their shape-dependent ORR. Then it summarizes the studies of alloy and core–shell NPs with controlled electronic (alloying) and strain (geometric) effects for tuning ORR catalysis. It further provides a brief overview of ORR catalytic enhancement with Pt-based NPs supported on graphene and coated with an ionic liquid. The review finally introduces some non-Pt NPs as a new generation of catalysts for ORR. The reported new syntheses with NP parameter-tuning capability should pave the way for future development of highly efficient catalysts for applications in fuel cells, metal-air batteries, and even in other important chemical reactions.

From the Contents

1. Introduction

The ever-increasing use of fossil fuels, coupled with the limited supply of these natural resources, has motivated the serious search for renewable and sustainable sources of energy.[1] Fuel cells are a common type of energy conversion device developed for future energy applications. Among various forms of fuel cells designed and tested, proton exchange membrane fuel cells (PEMFCs) feature high energy density, low operation temperature, and low environmental impact, and are a promising technology to power portable electronic devices, transportation vehicles, and stationary grids.[1,2] Figure 1 illustrates a typical PEMFC design, in which fuel (hydrogen, H_2) is oxidized at the anode, and oxygen (O_2) is reduced at the cathode, thus converting the chemical energy stored in H_2 into electrical energy. In such a fuel-cell device, the fuel can be any of hydrogen, methanol, ethanol, or formic acid, whereas highly electronegative O_2 is chosen to receive the electrons released from the fuel.[3] To achieve the desired energy output, a proton-exchange membrane based on Nafion, a copolymer of tetrafluoroethylene and perfluoro-2-(fluorosulfonylethoxy) propylvinylether, is used to separate the anode and cathode and to allow protons to migrate from anode to cathode to neutralize the reduced oxygen.[4] Overall, between the fuel oxidation reaction and the oxygen reduction reaction (ORR), electrons flow outside the cell to power electronic devices and protons migrate from anode to cathode inside through the Nafion membrane to complete the charge flow in the circuit.[5]

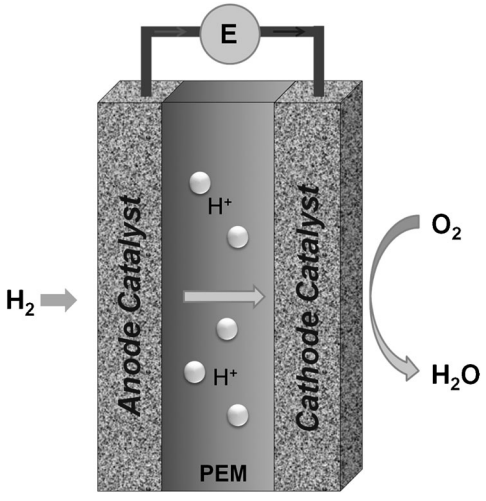

Figure 1. A typical PEM fuel cell with H_2 as fuel.

Despite their great potential as an efficient device to convert chemical energy into electric energy, PEMFCs do have their own serious limitations that prevent them from being scaled-up for commercial applications.[4] Both the fuel oxidation reaction and the ORR need a catalyst to lower their electrochemical over potentials and to obtain high voltage output, and platinum (Pt) has been the universal choice of catalyst for both reactions.[6,7] However, Pt is not an inexpensive metal to use; an industrial ORR catalyst with Pt nanoparticles (NPs) supported on carbon accounts for over 55% of the cost of a fuel-cell stack.[2] Furthermore, Pt NPs are subject to dissolution, coalescence, and poisoning under fuel-cell reaction conditions, thus reducing both the active catalyst surface area and the catalytic efficiency, which leads to an undesired increase in over potentials for fuel-cell reactions, especially for ORR.[8–12] Today, the lifetime of the state-of-art Pt catalyst maintaining high fuel-cell performance is far less than the 5000 h set as the year 2017 target by the US

[*] Dr. S. Guo,[+] S. Zhang,[+] Prof. S. Sun
Department of Chemistry, Brown University
Providence, RI 02912 (USA)
E-mail: ssun@brown.edu
[+] These authors contributed equally to this work.

Department of Energy (DOE).[13] This has posed tremendous challenges in the development of Pt-based catalysts for practical fuel-cell applications, and new innovative approaches to highly efficient fuel-cell catalysts is now desperately needed.

Recent advances in chemical synthetic methods have led to the formation of Pt-based NPs with precise controls of size, shape, compositions and structure. This allows detailed studies of the oxygen reduction reaction (ORR) for catalytst optimization. This review highlights the recent efforts in rational syntheses of Pt-based elemental, alloy, and multimetallic core–shell NPs, as well as some non-Pt catalysts for enhanced ORR catalysis. Despite the fact that the NP catalysts developed thus far have not reached a level where they can replace the current commercial Pt catalysts for fuel cell applications, the reported synthetic methods do provide a potential solution for catalyst optimization and may lead to a future breakthrough in catalyst development, not only for fuel cells, but also for other energy devices (such as metal–air batteries), and even for other important chemical reactions.

2. The ORR in General and Its Electrochemical Evaluation

The ORR involves a multi-electron transfer process in which O_2 is converted into H_2O or OH^-, depending on the solution used in the electrochemical studies.[14] In an acidic solution, O_2 can be reduced in a $4e^-$ process and converted into H_2O: $O_2+4H^++4e^-\rightarrow 2H_2O$. O_2 may also undergo a partial $2e^-$ reduction to form hydrogen peroxide, H_2O_2, followed by another $2e^-$ reduction to convert H_2O_2 into H_2O: $O_2+2H^++2e^-\rightarrow H_2O_2$; $H_2O_2+2H^++2e^-\rightarrow 2H_2O$. In alkaline solution, O_2 can be reduced by a $4e^-$ process to form hydroxide, OH^-: $O_2+2H_2O+4e^-\rightarrow 4OH^-$, or by two $2e^-$ processes to form HO_2^- and then OH^-: $O_2+H_2O+2e^-\rightarrow HO_2^-+OH^-$; $HO_2^-+H_2O+2e^-\rightarrow 3OH^-$.[15] In the common acid and alkaline solutions, ORR on a Pt catalyst surface usually follows the $4e^-$ pathway; but the true nature of the ORR process on a Pt surface is complicated and not well understood. Under common ORR conditions, O_2 may be converted into different intermediates, such as oxygenated (O*), hydroxyl (OH*) and superhydroxyl (OOH*) species, which are very difficult to detect experimentally. Recent density functional theory (DFT) calculations[16] show that, at high oxygen coverage, the ORR tends to follow an associative mechanism, in which OOH* is first formed and then O–O is cleaved; whereas, at low oxygen coverage, the ORR follows a dissociation mechanism in which the O–O bond is cleaved before OH* is formed.

To evaluate the ORR process electrochemically, the NP catalyst is usually dispersed in a mixture of water, isopropyl alcohol, and Nafion (5%) with a volume ratio of 4:1:0.025%, and deposited on a glassy carbon (GC) rotating disk electrode (RDE).[17] Depending on the area of the RDE used, the Pt loading is controlled in the range of 10–50 $\mu g\,cm^{-2}$ to ensure a thin layer of NP deposition on the electrode surface.[17] More catalyst loading can lead to the formation of an overly thick ($>1\,\mu m$) catalyst agglomerate, resulting in excessive mass-transport loss[17,18] and large uncertainty in qualifying catalytic activities.[19,20]

The electrochemical properties of the catalyst in an N_2- or Ar-saturated acidic solution (either 0.1 M $HClO_4$ or 0.5 M H_2SO_4) are first studied by cyclic voltammetry to obtain a cyclic voltammogram (CV) and to determine the electrochemically active surface area (ECASA) of the Pt catalyst. In a cathodic scanning process, H^+ is first reduced to H_2 adsorbed on the catalyst surface, and the related area under the current–potential (I–V) curve is referred to as the H_2 adsorption region. The adsorbed H_2 is oxidized in an anodic scanning process, which regenerates H^+, and the related area covered by the I–V curve is referred to as the H_2 desorption region. The H_2 desorption area, surrounded by the I–V curve and the potential scanning baseline, is integrated to obtain the ECASA.[21] In the calculation, electric charge is assumed to be $210\,mC\,cm^{-2}$ Pt after double-layer correction.[22] ORR activities are measured in an O_2-saturated acid or alkaline solution with the RDE rotating at a certain speed (usually 1600 rpm) and a potential sweep of 1.05–0 V vs. reversible hydrogen electrode (RHE) at rates of 5–20 $mV\,s^{-1}$ to minimize the interference from capacitive currents. From the ORR polarization curves of two kinds of catalysts under the same Pt loading and measurement conditions, half-wave potentials ($E_{1/2}$) of these two catalysts can be obtained and used to qualitatively determine the catalyst activity (Figure 2); the higher the potential, the better the ORR activity. For a more quantitative comparison, the kinetic current at 0.9 V (vs. RHE) is first obtained from the ORR polarization curve according to the Levich–Koutecky equation:[17,18]

$$1/i = 1/i_k + 1/i_d \quad (1)$$

Shaojun Guo received his B.Sc. in chemistry from Jilin University (2005). He joined the group of Prof. Erkang Wang and Prof. Shaojun Dong at the Changchun Institute of Applied Chemistry and received his Ph.D. degree in January 2011. He is currently a postdoctoral research associate in the Department of Chemistry at Brown University under the supervision of Prof. Shouheng Sun. His research interests are carbon and metal nanomaterials for electrochemical and analytical applications.

Sen Zhang received his B.Sc. in chemistry from the University of Science and Technology of China (USTC, Hefei, China) in 2008. He has been pursuing his Ph.D. under the supervision of Prof. Shouheng Sun in the Department of Chemistry at Brown University since 2009. His research interests are the synthesis of composite nanomaterials and their magnetic and catalytic applications.

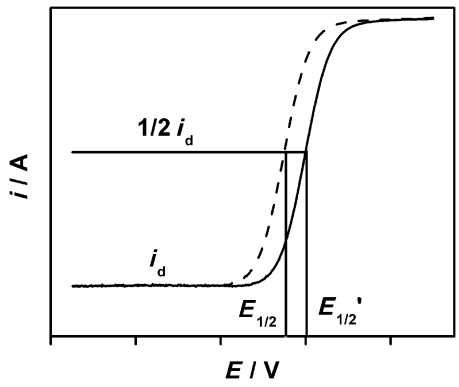

Figure 2. Typical ORR polarization curves of two different catalysts and the parameters used to qualitatively compare their activity.

where i is the current obtained experimentally, i_k is the mass-transport free kinetic current and i_d is the diffusion-limited current, as indicated in Figure 2. The specific activity of a NP catalyst can be determined by normalizing the i_k with its Pt ECASA. From the same experimental data, one can also determine the mass activity of the catalyst by normalizing the i_k with the Pt loading. The efficiency of a new catalyst can be evaluated by comparing its specific and mass activities with those obtained from the known "standard" Pt NP catalyst under the same measurement conditions.

Catalyst durability is tested by cycling the potentials over 0.6–1.05 V (vs. RHE) in O_2-saturated 0.1 M $HClO_4$ or 0.5 M H_2SO_4 solution. More than 4000 cycles are now routinely used in the literature, and the shift of the ORR polarization curve and the ECASA change of the NP catalyst before and after these potential cycles are compared to measure the durability of the NP catalyst. The smaller the shift and the ECASA change, the better the durability. In alkaline solution, the rate of the time-dependent current drop measured at a constant potential (usually half-wave potential) is usually used to estimate the durability of a NP catalyst.[23,24]

3. Pt NPs: Shape-Controlled Synthesis

Studies on single-crystalline thin films of face centered cubic (*fcc*) Pt have revealed that the ORR activity on Pt varies on different crystal planes. In a H_2SO_4 solution, this activity increases in the order (111) < (100).[25,26] This difference is caused by the stronger adsorption of sulfate anion (SO_4^{2-}) on Pt (111) versus on Pt (100). This strong sulfate absorption deactivates the Pt (111) surface, thus limiting its O_2 adsorption and activation capability.[26] However, when the ORR is tested in a $HClO_4$ solution with $[ClO_4]^-$ only weakly adsorbed on Pt (111), the Pt (111) surface becomes more active than the (100) one. These model studies indicate that a Pt NP catalyst with a cubic shape should be more active for ORR in H_2SO_4 and those with an octahedral (or tetrahedral, or icosahedral) shape should be ideal for ORR in $HClO_4$. It is therefore important to synthesize Pt NPs with controlled shapes to enhance ORR catalysis in the commonly used acid media.

Shouheng Sun received his Ph.D. in Chemistry from Brown University in 1996. He was a postdoctoral fellow from 1996–1998 and a research staff member from 1998–2004 at the IBM T. J. Watson Research Center. He joined the Chemistry Department of Brown University in 2005. He is now the Professor of Chemistry and Engineering at Brown. His research interests are in nanomaterials synthesis, self-assembly, and applications in catalysis, nanomedicine, and energy storage.

Fcc-Pt NPs normally adopt a polyhedral shape with their surface surrounded by low-index planes of {111} and {100} because this shape lowers the overall surface energy and makes the NPs thermodynamically more stable.[27] One way to achieve the desired shape control in Pt NP synthesis is to control the NP growth direction through the binding difference of a surfactant molecule on a crystal plane. This is nicely demonstrated in the synthesis of Pt NPs with tetrahedral, cubic, and truncated octahedral shapes through the reduction of K_2PtCl_4 by H_2 in an aqueous solution.[28] The Pt NP shapes were controlled by sodium polyacrylate or polyvinylpyrrolidone. At a high polymer concentration (0.4 mM), tetrahedral Pt NPs were produced, whereas at a low concentration (0.08 mM), selective growth onto {111} facets was achieved, and truncated octahedral and even cubic Pt NPs were obtained. Pt NP shape can also be controlled by reaction temperature. For example, Pt NPs were obtained by the reduction of $[Pt(acac)_2]$ (acac = acetylacetonate) in the presence of a small amount of $[Fe(CO)_5]$.[29,30] The injection of $[Fe(CO)_5]$ at 180 °C induced the fast nucleation and growth of Pt NPs, leading to the formation of 3 nm Pt NPs with the thermodynamically favored polyhedral shape. Injecting $[Fe(CO)_5]$ at 160 °C or 120 °C slowed down the rate of nucleation and growth, leading to the formation of larger NPs with (100) planes on the NP surface. As a result, by tuning the NP nucleation and growth temperatures, 3 nm polyhedral Pt NPs, 5 nm truncated cubic Pt NPs, and 7 nm cubic Pt NPs were synthesized, as shown in Figure 3 A–C.[29] Studies on ORR catalysis in H_2SO_4 solution (0.5 M) indicated that the cubic Pt NPs had much better activity than the polyhedral and truncated cubic NPs, as shown by their CVs and ORR polarization curves (Figure 3 D and E). The cubic Pt NPs show strong H_2 adsorption/desorption on their (100) planes at 0.22 V vs. normal hydrogen electrode (NHE; Figure 3 D) and generate four times higher specific current density than the polyhedral and truncated cubic Pt NPs around the half-wave potential (Figure 3 E).

High-index planes with a larger number of atoms at the steps, edges and kinks may also show higher electrocatalytic activity.[31–33] This is demonstrated in the study of 15–40 nm concave Pt NPs.[32] These NPs were synthesized by a slow reduction of a Pt pyrophosphato complex, which was achieved by adding the complex to the reaction system by a syringe pump. The slow Pt reduction allowed a selective overgrowth of Pt atoms on the corner and edge. The growth process was further optimized by using Br^- to block the {100}

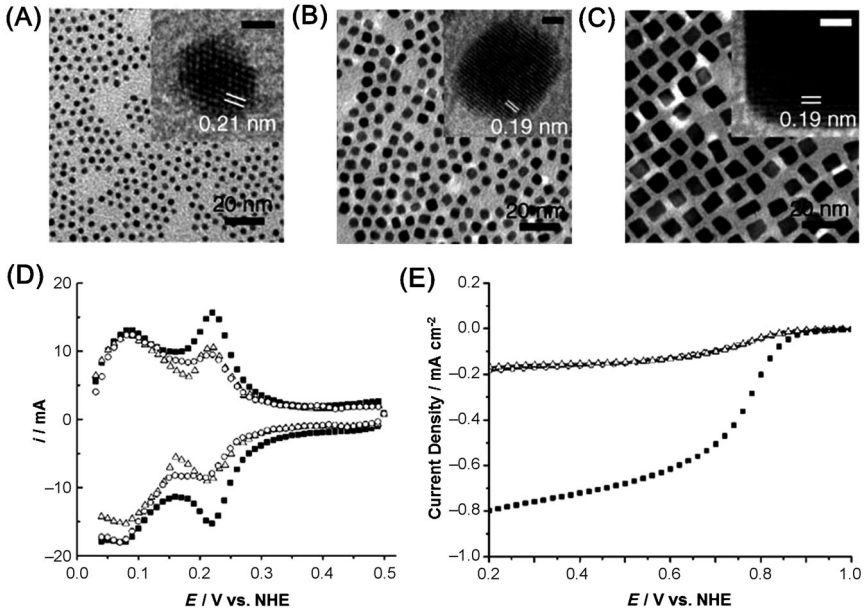

Figure 3. Representative TEM images of Pt NPs. A) 3 nm polyhedral, B) 5 nm truncated cubic, and C) 7 nm cubic. Insets show representative HRTEM images of the corresponding single NPs: A) Pt(111), B) Pt(100), and C) Pt(100) lattice fringes. All inset scale bars are 1 nm. D) CVs and E) ORR polarization curves of different Pt NPs: polyhedron (○), truncated cube (△), cube(■). Adapted from Ref. [29].

4.1. Controlled Synthesis of MPt NPs

The key to the success of solution-phase synthesis of monodisperse MPt NPs is to control the nucleation and growth of two metals with different redox properties. Under normal reduction conditions, a Pt salt tends to be reduced more easily than an early transition metal one, thus leading to the formation of a mixture of Pt and M NPs. This problem is solved by controlling the reaction chemistry, surfactant binding, and heating, as demonstrated in the synthesis of FePt NPs. These FePt NPs were prepared by the high-temperature solution-phase thermal decomposition of $[Fe(CO)_5]$ and reduction of $[Pt(acac)_2]$ in the presence of oleic acid (OA) and oleylamine (OAm).[37a] The simultaneous nucleation and growth of FePt was achieved by first heating the reaction mixture at 200 °C followed by the growth of FePt NPs at higher temperature. Under such controlled synthetic conditions, $[Fe(CO)_5]$ decomposed to carbon

facets. By controlling the KBr concentration, cuboctahedral and cubic Pt NPs could also be produced. As shown in Figure 4 A, the concave NPs are enclosed mainly by {720} as well as some {510} and {830} facets. Figure 4 B compares the specific ORR activities of these Pt NPs. The concave Pt NPs have more than three and two times greater ORR activity than the Pt cubes and cuboctahedra, respectively, thus suggesting the advantage of high-index facets in ORR catalysis. However, the concave Pt NPs have a relatively low mass activity owing to their large sizes. Even smaller NPs with high-index facets need to be synthesized before the true nature of their ORR enhancement can be revealed.

4. MPt Alloy NPs

Studies on crystalline thin films reveal that the addition of an early transition metal (M) to Pt can improve atomic and electronic structures of Pt and enhance its catalytic performance. Density function theory (DFT) calculations further indicate that alloying M with Pt downshifts the d-band center of the Pt catalyst, leading to a lower degree of adsorption of oxygenated spectator (blocking) species (such as OH^-) and increases the number of active sites accessible to oxygen.[34,35] The specific activities of the MPt alloys show a volcano-type relation with the alloy d-band center position, with M = Fe, Co, and Ni having much better ORR activities than any other MPt or Pt.[36] It is therefore critically important to synthesize alloy MPt NPs with tunable NP size, shape, type of M, and M/Pt composition to tune NP catalysis for ORR.[37–42]

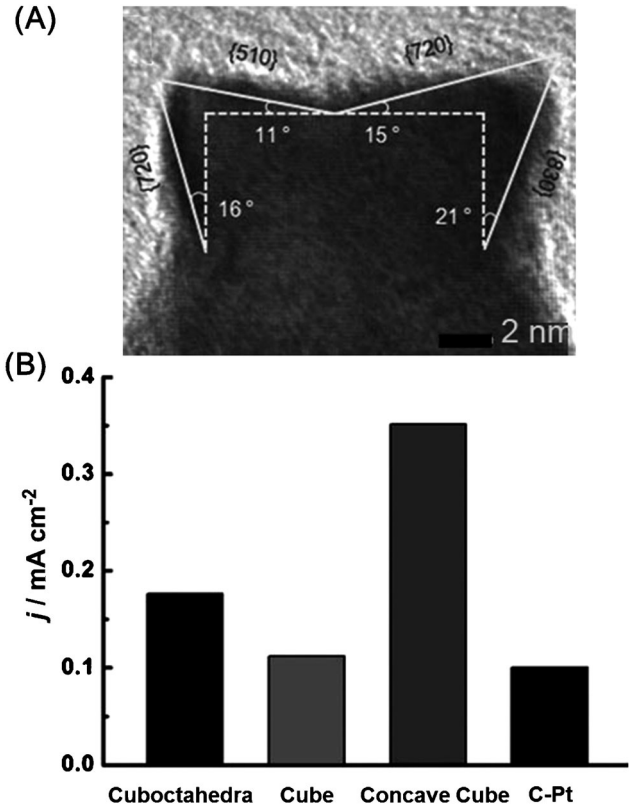

Figure 4. A) HRTEM image of a part of a Pt concave nanocube. B) Specific activities of different NPs at 0.9 V (vs. RHE). The metal loading of each NP catalyst on the GC electrode was 15.3 mg cm^{-2}. Adapted from Ref. [32].

monoxide and Fe, and [Pt(acac)$_2$] was reduced by 1,2-alkanediol, or by Fe generated from [Fe(CO)$_5$] decomposition, to Pt.[37b] FePt NPs could also be produced by co-reduction of Fe and Pt salts.[37c,d] Under similar reaction conditions, and by tuning the molar ratio of the two precursors (or the surfactant to precursor), the sequential addition of the precursors, or even the heating ramp rate, various MPt NPs with controlled size, shape, and composition have been produced.[42]

4.2. Size-Dependent ORR Activities of the MPt NPs

Previous studies on single-component Pt NPs have shown that their ORR catalysis is NP-size dependent, with the smallest (ca. 3 nm) Pt NPs having the best activity.[43] Owing to the M effect, the MPt alloy NPs have a different trend for their size-dependent catalytic properties.[36] This is demonstrated in $CoPt_3$ NPs with controlled sizes of 3–9 nm. The NPs were synthesized by thermal decomposition [$Co_2(CO)_8$] and reduction of [Pt(acac)$_2$] with 1,2-tetradecanediol in the presence of 1-adamantanecarboxylic acid and a large excess of OAm.[44,45] 1-adamantanecarboxylic acid was chosen to stabilize CoPt NPs by its steric effect and [$Co_2(CO)_8$] was added at a designated pre-heating temperature to control the $CoPt_3$ NP sizes.[44] Figure 5 A–D shows the representative TEM images of the $CoPt_3$ NPs obtained by adding [$Co_2(CO)_8$] at 225, 200, 170, and 145 °C, respectively. Studies on the ORR catalysis of these NPs supported on carbon (C-$CoPt_3$) indicated that their ORR specific activities increased, whereas their specific surface area decreased, with the NP sizes (Figure 5 E). As a result, their ORR mass activities showed a volcano-type relation with the NP sizes (Figure 5 F).

4.3. Composition-Dependent ORR Activities of MPt NPs

The successful synthesis of the monodisperse MPt NPs with rational control over the M and M/Pt ratio allows detailed studies of the M and M/Pt composition effect on NP catalysis for ORR. In a recent study, monodisperse 5 nm $FePt_3$, $CoPt_3$, and $NiPt_3$ NPs were synthesized and tested for their ORR catalytic activity.[46] Figure 6 A shows a typical TEM image of the monodisperse $FePt_3$ NPs. The MPt_3 NPs are much more active than the Pt catalyst, with their catalytic performance showing a volcano-type dependence on the type of M employed (Figure 6 B). Among these three kinds of alloy NP catalysts, the $CoPt_3$ NPs have the highest specific and mass activity, which is consistent with what has been observed from thin film studies.[36] The M/Pt composition effect on ORR catalysis was demonstrated in the FePt and NiPt NP systems. The ORR activities of the 4 nm *fcc*-Fe_xPt_{100-x} ($x = 63$, 58, 54, 42, 15, and 0) NPs were dependent on Fe, Pt composition with $Fe_{42}Pt_{58}$ NPs being the most active.[47] Similarly, monodisperse 5 nm Ni_xPt_{1-x} NPs were synthesized by the co-reduction of [Pt(acac)$_2$] and nickel acetate ([Ni(ac)$_2$]) with x controlled by the molar ratios of the Pt and Ni precursors.[48] Their composition-dependent ORR activities showed that the NiPt or $NiPt_2$ NPs were more active than any other NiPt NPs.

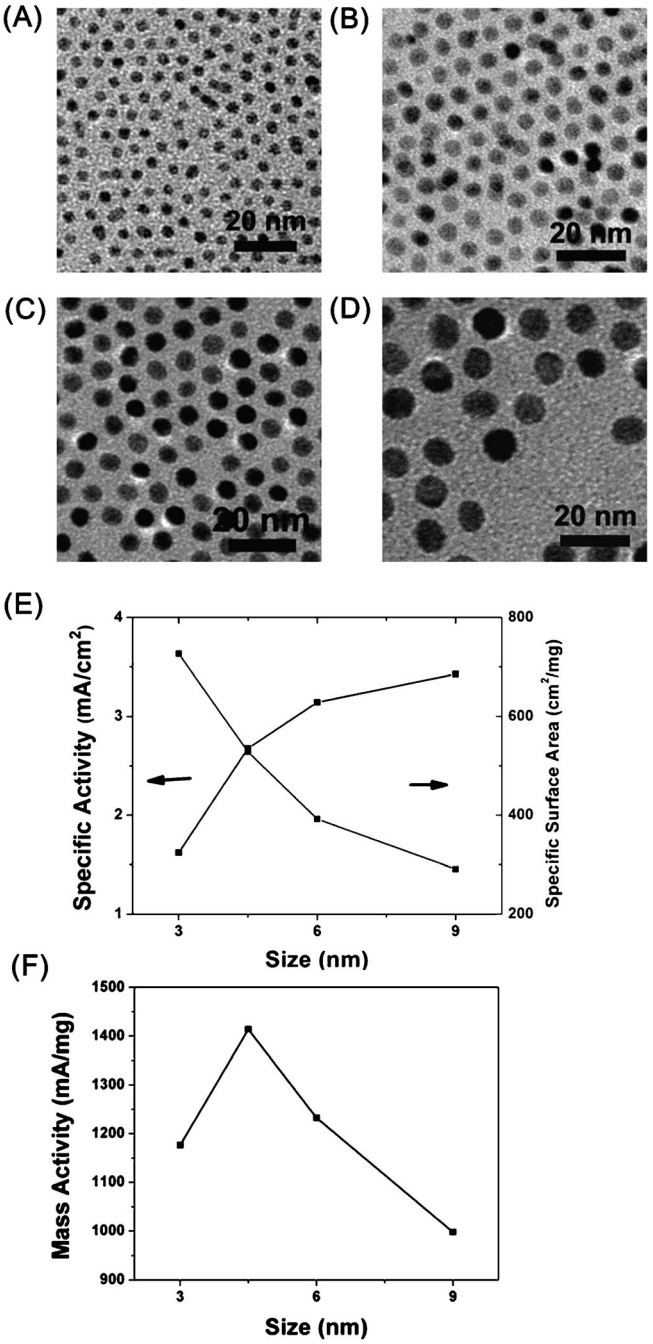

Figure 5. A–D) TEM images of 3 nm (A), 4.5 nm (B), 6 nm (C), and 9 nm (D) $CoPt_3$ NPs synthesized by adding [$Co_2(CO)_8$] at 225, 200, 170, and 145 °C, respectively. E) Specific activity (black) and specific surface area (gray) of the C-$CoPt_3$ NPs vs. NP sizes. F) Mass activity of the C-$CoPt_3$ NPs vs. NP sizes. Adapted from Ref. [44] with permission by the American Chemical Society.

4.4. Shape-Dependent ORR Activities of the MPt NPs

Recent thin film studies also showed that $NiPt_3$(111) had an ORR activity tenfold higher than Pt(111), and 90-fold higher than the current state-of-the-art Pt catalyst in $HClO_4$ solution.[34] This indicates that MPt NPs surrounded by (111) facets should be more active for ORR in $HClO_4$. This is nicely

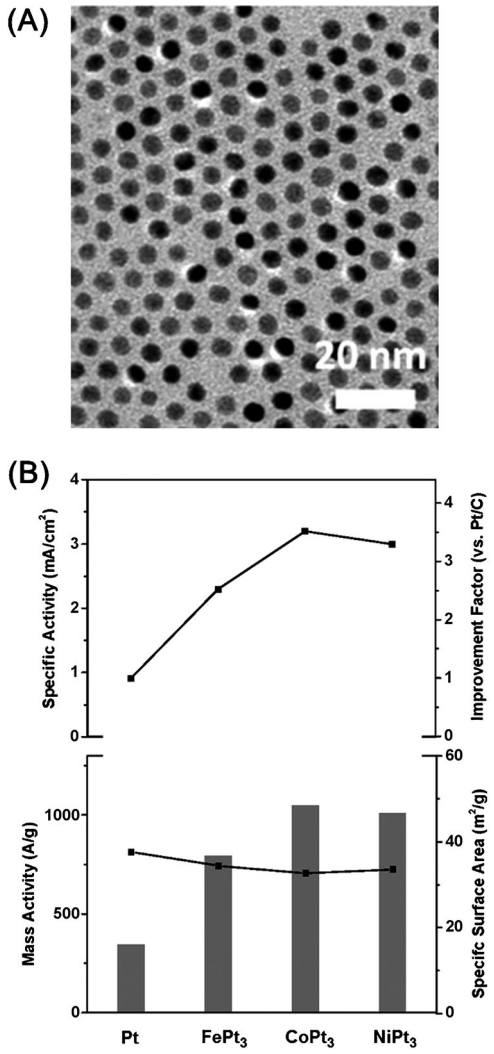

Figure 6. A) TEM image of 5 nm $FePt_3$ and B) M-dependent specific activity, mass activity, and specific surface area of MPt_3 NPs. Adapted from Ref. [46] with permission by the American Chemical Society.

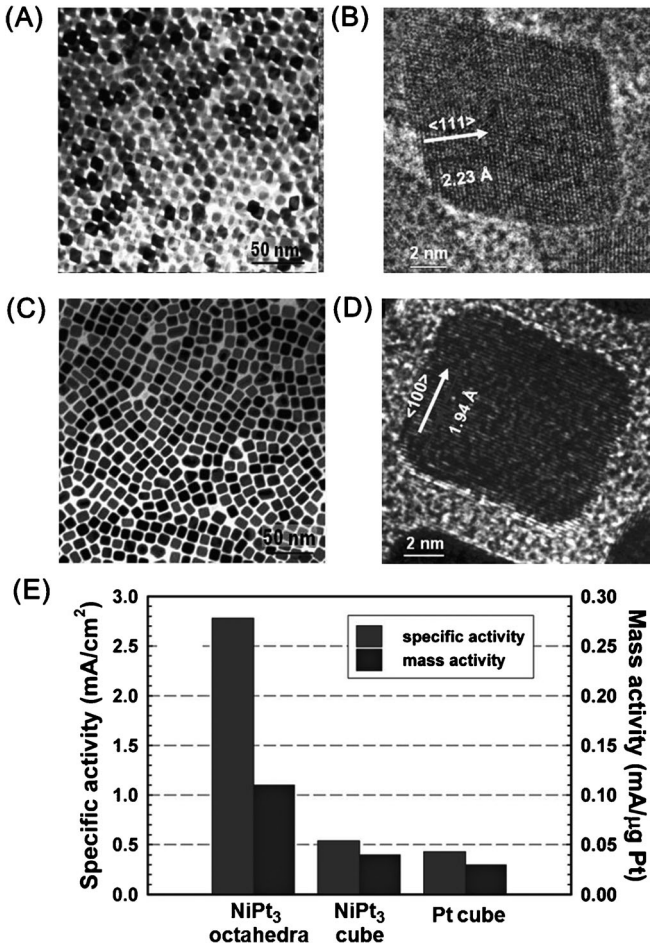

Figure 7. A, C) TEM and B, D) HRTEM images of the $NiPt_3$ nanooctahedra (A, B) and nanocubes (C, D). E) ORR activities of the $NiPt_3$ nanooctahedra, $NiPt_3$ cubes, and Pt cubes. Specific activity and mass activity were all measured at 0.9 V (vs. RHE) at 295 K. Adapted from Ref. [51] with permission by the American Chemical Society.

demonstrated in the studies of a series of $NiPt_3$ nanooctahedra,[42a,49–51] truncated nanooctahedra,[50,52] and nanoicosahedra.[53] The monodisperse octahedral $NiPt_3$ NPs were prepared by the reduction of $[Ni(acac)_2]$ and $[Pt(acac)_2]$ with $[W(CO)_6]$.[51] Adding a trace amount of $[W(CO)_6]$ seemed to be important to initiate the nucleation and growth of the NiPt NPs into a specific shape, and tungsten could not be detected in the final NP product. Figure 7 A–D shows the typical TEM (**A**, **C**) and HRTEM (**B**, **D**) images of the $NiPt_3$ nanooctahedra and nanocubes. Their ORR catalysis was studied in $HClO_4$ solution (0.1 M) and summarized in Figure 7 E. The specific activity of the $NiPt_3$ nanooctahedra is 5.1 times that of the $NiPt_3$ nanocubes and ca. 6.5 times that of the Pt nanocubes. A similar ORR activity trend was also observed from the truncated nanooctahedra, with those surrounded by the most (111) facets having the best ORR activity.[52] To test more shape effects on NP catalysis for ORR, 13 nm icosahedral (Ih) $NiPt_3$ NPs were synthesized by CO gas coreduction of $[Pt(acac)_2]$ and $[Ni(acac)_2]$, as shown in Figure 8 A.[53] Their ORR specific activity was about 50 % higher than that of the octahedral (Oh) $NiPt_3$ NPs (Figure 8 B). This activity difference observed from the $NiPt_3$ NPs with same composition but different shapes seems to infer that surface strain plays an important role in their ORR enhancement. It is apparent that both geometric (shape) and electronic (alloying) effects are involved in these NPs for their ORR catalysis enhancement. The shape-dependent ORR catalysis of other MPt NPs was also studied. For example, uniform cubic and spherical MnPt NPs were synthesized by the coreduction of $[Pt(acac)_2]$ and $[Mn(acac)_2]$.[40d] ORR activity studies of these cubic and spherical MnPt NPs in H_2SO_4 and $HClO_4$ revealed that the cubic MnPt NPs had higher ORR activity than the spherical MnPt NPs in H_2SO_4, whereas the spherical NPs were more active in $HClO_4$ solution; this further supports the conclusions obtained from both thin-film and Pt NP studies.

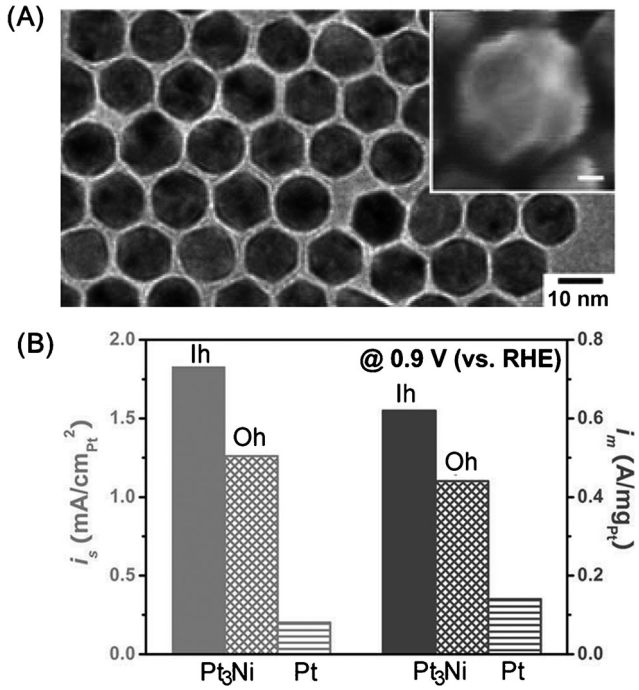

Figure 8. A) TEM and SEM (inset) images of $NiPt_3$ icosahedral NPs. B) Mass- and area-specific activities of the $NiPt_3$ icosahedral and octahedral NPs, and Pt reference catalysts measured at 0.9 V (vs. RHE). Adapted from Ref. [53] with permission by the American Chemical Society.

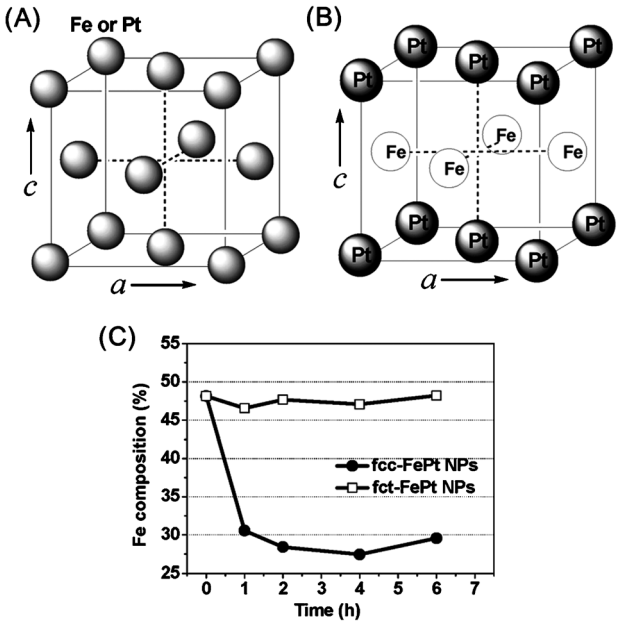

Figure 9. The unit cell of A) the chemically disordered *fcc*-FePt and B) the chemically ordered *fct*-FePt. C) Time-dependent composition changes of the *fcc*- and *fct*-FePt NPs in H_2SO_4 solution (0.5 M). Adapted from Ref. [56] with permission by the American Chemical Society.

4.5. Structure-Controlled Stability of MPt NPs under ORR Conditions

Despite the exciting observations made in studying MPt alloy NPs for ORR catalysis, there exists a serious concern when using these alloy NPs to catalyze ORR in an acidic solution: the alloy structure is chemically unstable and the M components of the MPt NPs are subject to fast dissolution. When this dissolution happens in the near-surface layers, a Pt-skeleton surface is formed.[54] This surface is rich in corner and edge sites and has more undercoordinated atoms, promoting the adsorption of oxygenated spectator species (such as OH^-) and blocking the adsorption/activation of O_2.[55] The easy dissolution of M and the formation of the Pt-skeleton structure make MPt NPs even less stable than Pt NPs under ORR conditions.

Recent studies on structure-controlled stability of the MPt NPs reveal that the chemical instability observed in MPt NPs originates from their chemically disordered *fcc* structure formed during solution-phase synthesis.[37f] In this *fcc* structure, M and Pt atoms randomly occupy the *fcc* crystal lattice, thus facilitating M dissolution in an acidic solution. One strategy to stabilize such MPt NPs is to convert their *fcc* structure into a chemically ordered face-centered tetragonal (*fct*) structure in which Pt and M are separated within the structure, forming the alternating layers of atomic arrays. This is illustrated in the study of the structure-induced stabilization of FePt NPs in acid.[37f,56] As synthesized from the organic solution phase reaction, the FePt NPs have an *fcc* structure (Figure 9A). Once annealed at high temperature (above 550 °C), the *fcc* structure can be converted into an *fct* structure (Figure 9B). These *fct*-FePt NPs are stable, without evident Fe loss, when suspended in H_2SO_4 solution for 6 h. In contrast, the *fcc*-FePt NPs show an instant Fe loss when they are exposed to the acidic solution (Figure 9C). As a result, the *fct*-FePt NPs are more efficient than the *fcc*-FePt NPs in catalyzing the ORR.[56]

5. Pt-Based Core–Shell NPs

Pt-based core–shell NPs are another new class of electrocatalysts studied for ORR. In this structure, a thin shell of Pt or Pt alloy is deposited on the non-Pt NP core and Pt usage is greatly reduced. More importantly, the activity and durability of the Pt shell can be enhanced by the structure-induced strain (geometry) and electronic (alloying) effects that are tunable by controlling core–shell composition, size, and shape. Various methods have been developed to prepare core–shell NPs. Herein, we summarize three common approaches to core–shell NPs with significantly enhanced ORR catalysis.

5.1. Core–Shell NPs from Galvanic Replacement

Pt monolayer (Pt_{ML}) was first deposited on single crystalline Pd substrate for ORR studies. This thin film version of the core–shell structure was made through a galvanic replacement reaction.[57] In this approach, a Cu monolayer was coated over the Pd thin film by an under-potential deposition (UPD) method. The monolayer Cu-covered Pd thin film was

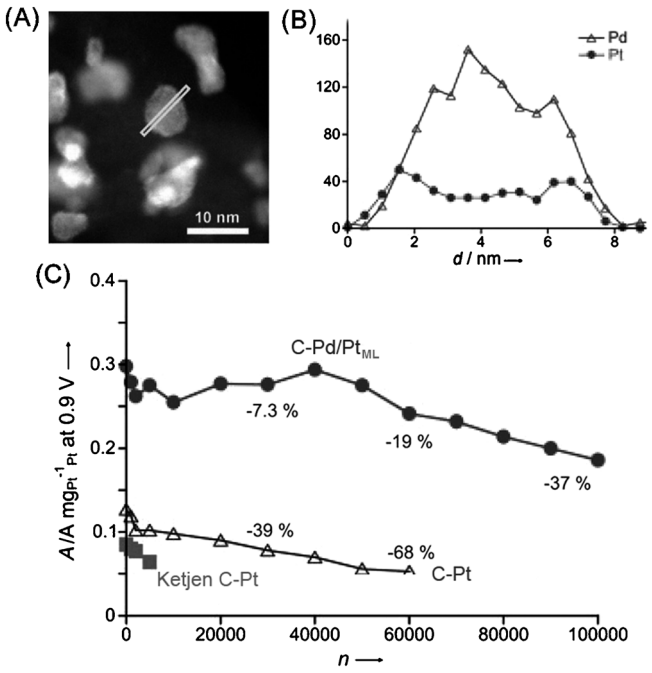

Figure 10. A) HAADF-STEM image and B) linear scan analysis of Pd/Pt_{ML} NPs. C) Mass activity of different catalysts for the ORR as a function of the number of potential cycles (*n*) during fuel cell testing. Adapted from Ref. [58].

immersed in K_2PtCl_4 solution to allow the galvanic replacement of Cu by Pt ($Cu + Pt^{2+} \rightarrow Cu^{2+} + Pt$). This technique was easily extended to NP systems, as shown in the synthesis of Pd/Pt_{ML} NPs and Pd_9Au_1/Pt_{ML} NPs.[58] Figure 10A and B shows the high-angle annular dark-field (HAADF) scanning transmission electron microscopy (STEM) images, along with the corresponding EELS spectrum of a Pd/Pt_{ML} NP. The studies on their catalysis for ORR indicated that these Pd/Pt_{ML} NPs had significantly enhanced mass activity and stability (tested after 100000 potential cycles between 0.7 V and 0.9 V with a 30 second dwelling time at 80 °C) versus the commercial 3.5 nm Pt catalyst (Figure 10C). This enhanced activity and stability of the Pd/Pt_{ML} NPs is believed to arise from Pt lattice compression on the Pd surface, causing a downshift of the d-band center of Pt and the decreased interaction of Pt with ORR intermediates. The Pd_9Au_1/Pt_{ML} NPs showed much improved stability owing to Au-induced resistance to the formation of Pd–OH and Pt–OH bonds under ORR conditions.

Results from the Pd/Pt_{ML} or PdAu/Pt_{ML} NPs infer that an early-transition-metal core may further increase the core–shell NP catalyst performance owing to electronic (metal redox property differences) and strain effects (metal lattice mismatch). Therefore, galvanic replacement has been applied extensively in depositing Pt_{ML} onto many different metallic NPs, including CoPd,[59] NiIr,[60] PtPb,[61] PdPb,[61] FePd,[61] NiRe,[62] and AuNiFe NPs.[63] For example, in the synthesis of AuNiFe/Pt_{ML} NPs, $AuNi_{0.5}Fe$ NPs were synthesized by thermal decomposition of a $[AuNi_{0.5}Fe(CN)_6]$ complex at 500 °C under a reducing atmosphere of H_2/Ar (15:85 v/v), and further used as a core to synthesize $AuNi_{0.5}Fe/Pt_{ML}$ NPs.[63] The $AuNi_{0.5}Fe/Pt_{ML}$ NPs showed a mass and specific activity of 1.38 A mg^{-1} Pt and 1.12 mA cm^{-2} Pt, respectively, both of which were several times higher than those of commercial Pt catalysts. Stability tests showed that the $AuNi_{0.5}Fe/Pt_{ML}$ NPs had no significant loss in activity after 15000 potential cycles. Recently, Pt_{ML} was even deposited on intermetallic PtPb, PdPb, and PdFe NPs[61] and $(Pt_{0.8}M_{0.2})_{ML}$ on Pd, Re, Os, Ir, Ru, or Rh to enhance catalyst stability and to further improve ORR catalysis.[64]

5.2. Seed-Mediated Growth to Core–Shell NPs

Seed-mediated growth is a common way to grow Pt shells over the monodisperse NPs.[65] In this synthesis, core NPs are first prepared and shell material is controlled to nucleate and grow around the core NPs. The successful synthesis of metallic core–shell NPs is often dependent upon the degree of crystallographic lattice matching between the core and shell components. A large crystal-lattice mismatch may lead to separate nucleation and growth unless special reaction conditions are applied, as demonstrated in the synthesis of core–shell metal/salt hybrid NPs.[66]

Synthesis of Pd/FePt NPs provides a good example of using a seed-mediated growth method to produce core–shell NPs with a uniform Pt shell coating.[67] Pd NPs (5 nm) were synthesized by reducing $[Pd(acac)_2]$ with borane *tert*-butylamine complex in the presence of OAm as a surfactant.[68] To apply the FePt coating, the OAm-coated Pd NPs were mixed with $[Fe(CO)_5]$ and $[Pt(acac)_2]$ in 1-octadecene (ODE), and thermal decomposition of $[Fe(CO)_5]$ and reduction of $[Pt(acac)_2]$ at 180 °C led to a tight and uniform FePt shell. These FePt shells were generated in a controlled fashion, producing thicknesses of 1 nm, 2 nm, and 3 nm by varying the precursor/Pd seed ratio. The Pd/FePt NPs exhibited an ORR activity in $HClO_4$ solution (0.1 M) that was dependent upon FePt shell thickness, with the 1 nm shell showing a much higher specific and mass-current density than the commercial Pt catalyst. More importantly, the core–shell NPs were more stable under ORR conditions than the Pt catalyst. They showed no noticeable change in morphology and activity after 10000 potential cycles in O_2-saturated $HClO_4$ solution (0.1 M).

The abovementioned ORR activity and durability increase is better demonstrated in Au/$FePt_3$ NPs.[69] In this study, the 7:1.5 nm Au/$FePt_3$ NPs were synthesized by mixing 7 nm Au NPs with $[Fe(CO)_5]$ and $[Pt(acac)_2]$ under conditions similar to the synthesis of Pd/FePt NPs. The 7 nm Au core and 1.5 nm uniform $FePt_3$ shell was characterized by HAADF-STEM, as shown in Figure 11A. The Au/$FePt_3$ NPs show mass activity enhancement of more than one order of magnitude over the Pt catalyst (Figure 11B). Moreover, the Au/$FePt_3$ NPs possess superior durability and show negligible morphology change, even after a stability test of 60000 potential cycles between 0.6 V and 1.1 V (vs. RHE) (Figure 11C,D), which is much better than Pt and $FePt_3$ NP catalysts under the same conditions. The experimental and theoretical study indicate that the superior stability of Au/$FePt_3$ NPs is strongly related to the core-hindered Pt place exchange mechanism; a well-known mechanism used to explain Pt dissolution caused by

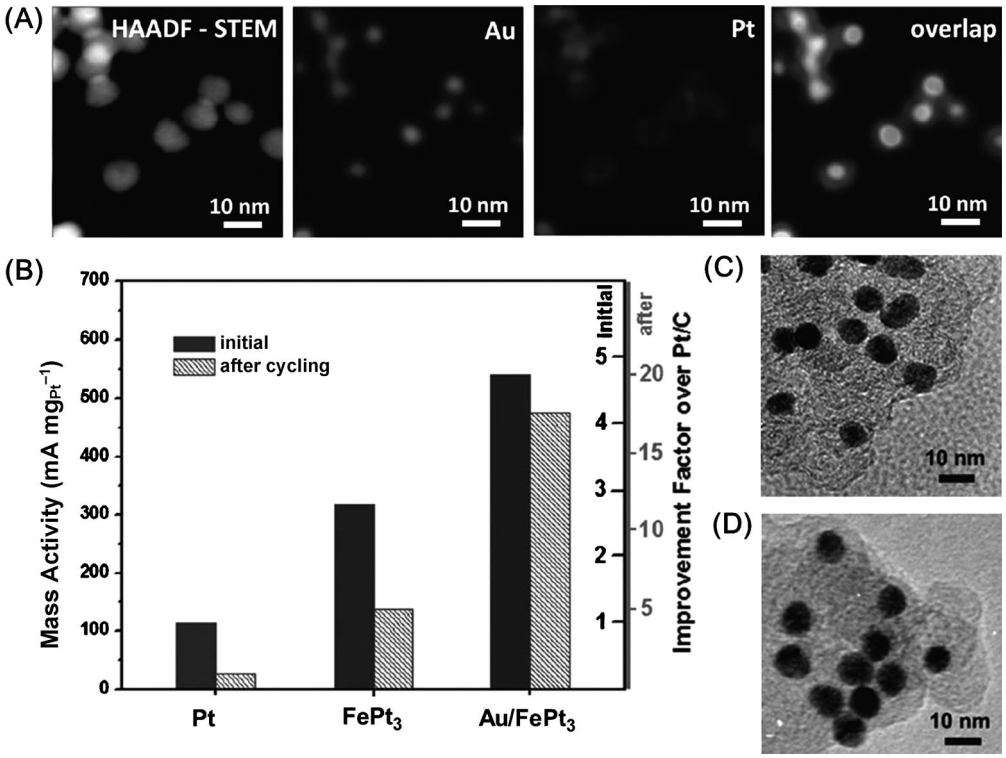

Figure 11. A) HAADF-STEM elemental mapping of Au, Pt, and a single Au/$FePt_3$ core–shell NP. B) Summary of the mass activities of different NPs before and after stability tests. C, D) TEM Images of the Au/$FePt_3$ NP catalysts before (C) and after (D) the stability tests. Adapted from Ref. [69] with permission by the American Chemical Society.

the migration of atomic oxygen from the surface to subsurface in ORR catalysis.[70,71] The existence of thermodynamically stable Au in the subsurface layer makes the formation of subsurface oxide energetically harder and thus prevents the dissolution of Pt. More recently, it was found that the composition of the core also had an important role in enhancing ORR.[72] AuCu alloy core NPs were synthesized by mixing [$Cu(acac)_2$] and Au NPs in OAm at 280 °C. In the process, [$Cu(acac)_2$] was reduced and deposited on the pre-synthesized Au NPs. Then, high temperature promoted diffusion of Cu into Au, thus forming AuCu NPs that were further used as the core for the synthesis of core–shell AuCu/Pt NPs.[72] Compared to Au/Pt core–shell NPs, the AuCu/Pt NPs showed superior catalytic activity and excellent stability towards the ORR. The results suggest that the Au component in the AuCu alloy core is crucial for stabilizing the Pt shell during the ORR, and the strain effect on the Pt shell induced by the smaller lattice of the AuCu core may be responsible for their superior catalytic activity for ORR.

5.3. Core–Shell NPs from Surface Dealloying of MPt NPs

Recently, surface dealloying of the alloy MPt NPs was introduced to make core–shell NPs for enhanced ORR performance.[73–76] This is demonstrated in the preparation of CuPt/Pt NPs from CuPt NPs.[73] CuPt NPs with different compositions ($Cu_{25}Pt_{75}$, $Cu_{50}Pt_{50}$, $Cu_{75}Pt_{25}$) were deposited on carbon supports, and were made through impregnation and thermal annealing of the mixture of C–Pt NPs and $Cu(NO_3)_2$ under a 4:96 H_2/Ar atmosphere. The CuPt NPs were electrochemically scanned over 0.05 V to 1.2 V in $HClO_4$ solution (0.1 M) to remove active Cu in the outer shell. After 200 potential cycles, CuPt NPs with a Pt-rich shell were formed. The dealloyed CuPt/Pt NPs were much more active than the Pt NP catalyst with a core–shell structure obtained from the $Cu_{75}Pt_{25}$ NPs with the best ORR activity (Figure 12A). Figure 12B shows the experimental ORR activity (in units of kT $\ln(j_{alloy}/j_{Pt})$, $T = 298$ K) of two families of the dealloyed CuPt NPs plotted as a function of strain, $(a_{shell}\text{-}a_{Pt})/a_{Pt}$, in the shell (gray and black trian-

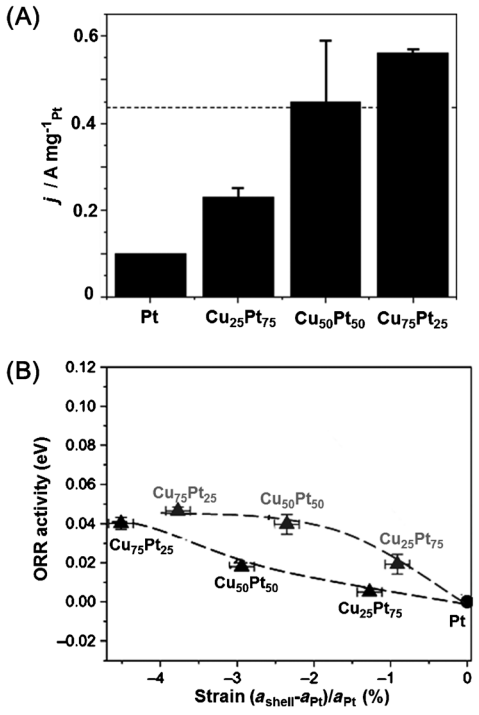

Figure 12. A) Mass activities of the dealloyed CuPt NPs and Pt NPs. B) The ORR activities of two families of dealloyed CuPt NPs plotted as a function of strain, $(a_{shell}-a_{Pt})/a_{Pt}$, in the NP shell. Adapted from Ref. [73] with permission by the Nature Publishing Group.

gles denote dealloyed CuPt NPs prepared at annealing temperatures of 800 °C and 950 °C, respectively). As the amount of Cu in the dealloyed CuPt NPs increases, the ORR activity increases accordingly. This is because the a_{shell} (the lattice parameter of Pt shell in CuPt/Pt core–shell NPs) is smaller than a_{Pt} (lattice parameter of bulk Pt). The compressed Pt–Pt distance in the Pt shell causes the downshift of the Pt d-band center and weakens bonding with oxygenated adsorbates. The Cu-rich $Cu_{75}Pt_{25}$ NPs amplify this strain effect and become the most active ORR catalyst among the three studied dealloyed core–shell NP catalysts.

The detailed surface structure change during the dealloying process is demonstrated in NiPt NPs.[77] Monodisperse NiPt NPs were synthesized and deposited on carbon support. Heat treatment at ca. 200 °C was used to remove the surfactant on the surface of NiPt. Further treatment with $HClO_4$ solution (0.1 M) led to Ni leaching from the surface of NiPt NPs, producing a skeleton-type surface structure. Thermal treatment at 400 °C converted the Pt-skeleton into a Pt-skin structure by surface relaxation and restructuring. Figure 13 A shows the representative HAADF-STEM images of the as-prepared (left), acid treated (middle), and acid treated/annealed (right) NiPt NPs. The composition line profiles of three NPs with different treatments are shown in Figure 13 B. It can be seen that the distribution of Pt and Ni in the as-prepared catalyst is highly intermixed and the sketched trend lines are almost identical, indicating a homogeneous alloy nature of the catalyst particles. The treated catalysts have substantially broader distribution of Pt than Ni, with a difference of ca. 1 nm for the acid treated and ca. 0.6 nm for the acid treated/annealed catalyst. This reveals that a multilayered Pt-rich surface structure is formed by acid treatment and preserved after annealing (Figure 13 C). The ORR test results of these three types of catalysts are shown in Figure 13 D and E. The acid-treated/annealed NiPt NPs show higher ORR activity than both the acid-treated NiPt and Pt NPs. After the stability test, the acid-treated/annealed NiPt NPs have only a 15 % loss in specific activity, in contrast to a 57 % loss for the acid-treated catalyst and a 38 % loss for the C-Pt catalyst. These indicate that the multilayered Pt-skin formation in the acid-treated/annealed NiPt NPs indeed provides complete protection of the Ni inside the catalyst and enables sustained high catalytic activity. The strategy has also been extended to MPt (M = Fe, Co) NPs. For example, the $CoPt_3$ NPs were annealed to form a Pt-rich shell by either heating in a CO environment or by electrochemical potential cycling in CO-saturated alkaline solution,[78] or through acid treatment by leaching of surface Co followed by thermal annealing to promote the formation of a complete Pt skin.[79] Similarly, core–shell NPs can also be prepared from the trimetallic alloy NPs of $Pt_3M_1M_2$ (M_1, M_2 = Fe, Co, Ni) NPs.[80,81] These core–shell NPs have consistently shown activity and durability enhancement relative to the commercial Pt NP catalyst.

6. Other Approaches to Active Pt-based NP Catalysts

6.1. Graphene Support Effects on NP Catalysis

Commercially available carbon particles with high surface area are usually employed as a support to maximize the activity of Pt-based NP catalysts. However, this kind of

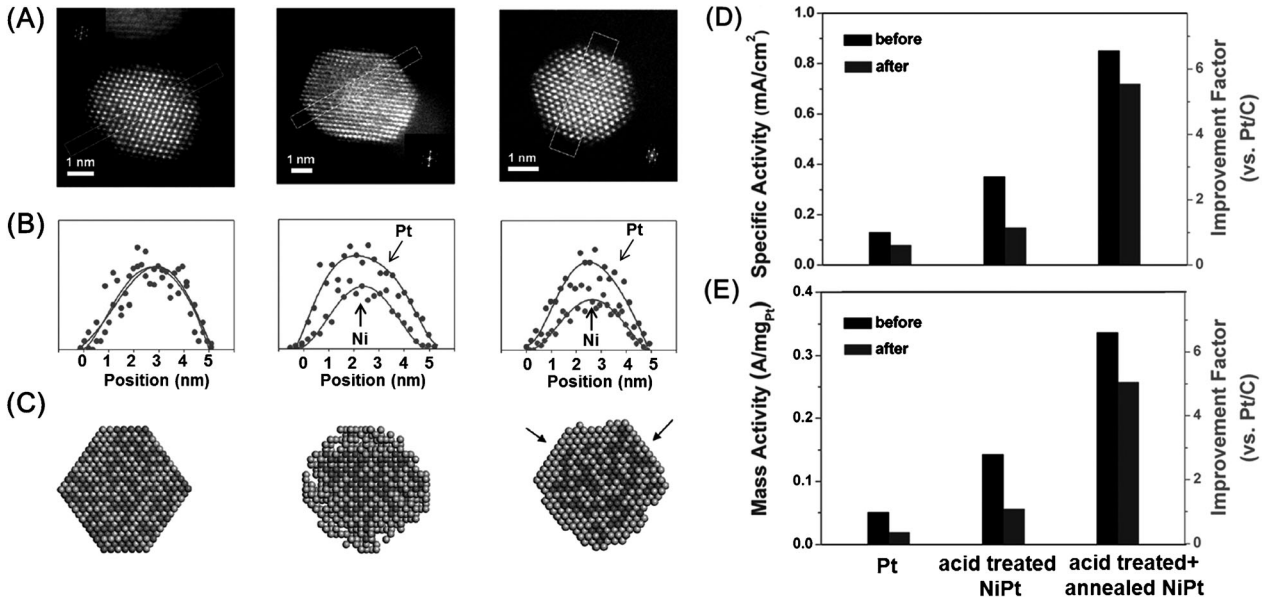

Figure 13. A) Representative HAADF-STEM images of NiPt NPs (left), acid treated NiPt NPs (middle), and acid-treated and annealed NiPt NPs (right). B) The composition line profiles obtained by energy-dispersive X-ray spectroscopy (EDX) with an electron beam scanning across the corresponding three NPs. C) Cross-sectional views of the corresponding three NPs depicted by atomistic simulation. D, E) Specific activity (D), mass activity (E), and durability studies for the C-Pt and C-NiPt catalysts in $HClO_4$ solution (0.1 M) at 0.95 V and 60 °C. Activity improvement factors vs. C-Pt before and after cycling are also shown for specific and mass activities in (D) and (E). Adapted from Ref. [77a] with permission by the American Chemical Society.

carbon support does not have long-range order in the graphitic lattice and may be poorly connected with the NP catalyst, thus leading to high electron-transfer resistance and an undesired increase in ORR overpotential. As a result, metal NP catalysts supported on this carbon tend to aggregate/sinter under the common ORR conditions, causing ORR activity degradation.[82] Moreover, this carbon support does corrode in the common ORR testing conditions, which aggravates the NP aggregation/sintering problems and further reduces the durability of the NP catalysts.[8]

Graphene (G) has been extensively studied as an alternative support to enhance NP catalyst activity and durability owing to its high surface area, high conductivity, high stability, and strong interaction with NPs.[83–91] G-Pt NP catalysts were initially made by chemical reduction of the Pt precursor directly onto the graphene surface.[85,86] ORR catalysis studies indicated that graphene as a support enhanced both Pt activity and stability. The stability of the Pt NPs were further improved by attaching Pt to indium tin oxide (ITO) NPs on graphene, forming metal-metal oxide-G triple junctions.[88a] Both experimental work and DFT calculations showed that the supported Pt NPs at the G-ITO-Pt triple junctions were more stable than the G-Pt NPs. A similar strategy was also applied to make G-CB-Pt NPs (CB = carbon black) to enhance ORR activity and durability.[88b] The accelerated durability tests revealed that G-CB-Pt NPs lose only 5% of their ECASA after up to 20000 cycles of stability testing, whereas the commercial C-Pt catalysts lose almost 50% of their ECASA after the same number of cycles. Here, the CB is believed to serve as an active site for recapture or renucleation of small Pt clusters, avoiding Pt loss into the electrolyte during the stability test.

Owing to the great potential shown by graphene as a support for ORR, various synthetic strategies have been explored to prepare G-MPt alloy NPs as ORR catalysts.[89,90] More recently, a solution-phase self-assembly method was developed to deposit monodisperse MPt NPs on graphene so that NP-G interaction can be better tuned for ORR.[91] In this self-assembly approach, 7 nm monodisperse $Fe_{58}Pt_{42}$ NPs were first synthesized, as shown Figure 14A, then, an equal amount of a dimethylformamide (DMF) solution of graphene and an *n*-hexane dispersion of the FePt NPs were mixed under sonication. The product was washed with ethanol, giving the G-FePt with the FePt NPs deposited fairly uniformly on graphene (Figure 14B). After removing the surfactant by treating with acetic acid (AA) at 70°C, FePt NPs on the graphene surface maintained their morphology (Figure 14C). The ORR polarization curves of the G-FePt, C-FePt, and commercial C-Pt are shown in Figure 14D. The ORR specific activity of different catalysts increases in the order G-FePt > C-FePt > C-Pt in the potential range of 0.512–0.557 V (vs. Ag/AgCl). When the G-FePt NPs were treated at 100°C, their ORR activity was increased further to about 2, 4, and 6 times higher than the AA-treated G-FePt NPs, the C-FePt NPs, and the commercial C-Pt NPs, respectively (Figure 14E). The G-FePt NPs were also fairly stable for ORR, as there was little change in ORR polarization curves before and after 10000 electrochemical potential sweeps in the range of 0.4–0.8 V (vs. Ag/AgCl) in O_2-saturated $HClO_4$ solution (0.1M; Figure 14F). These indicate that graphene is indeed a promising support to improve NP activity and durability for ORR.

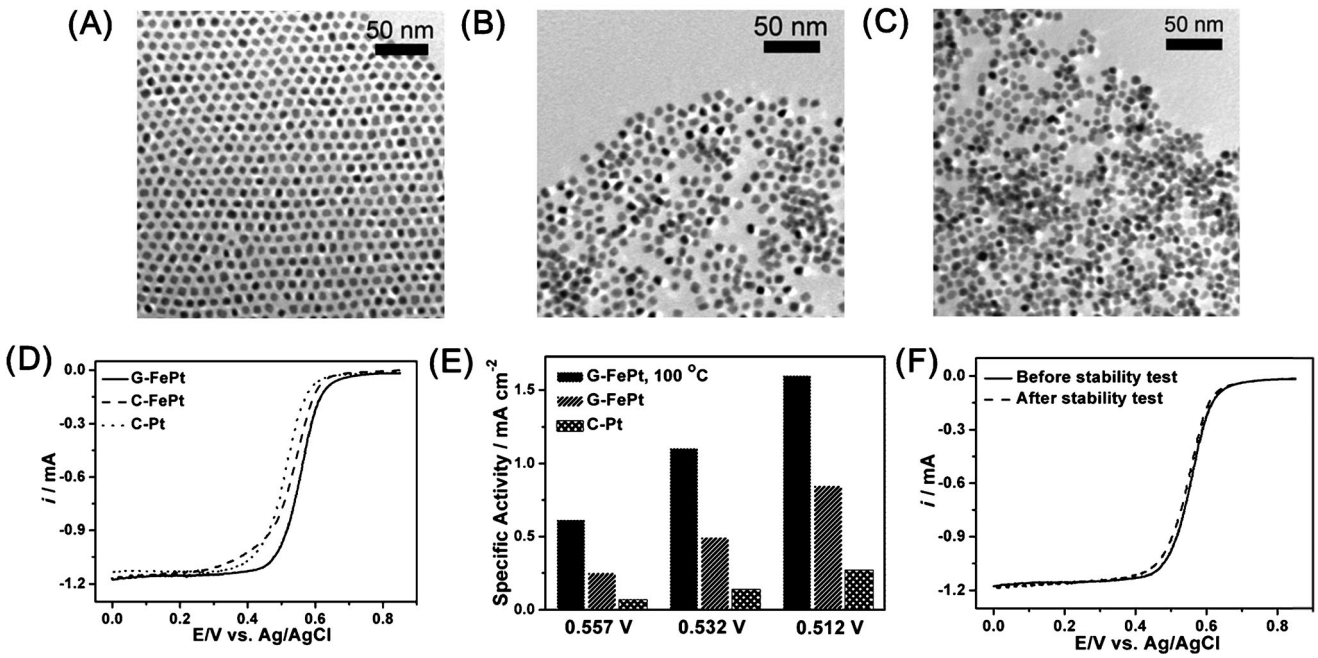

Figure 14. TEM images of A) 7 nm $Fe_{58}Pt_{42}$ NPs assembled on an amorphous carbon surface, B) $Fe_{58}Pt_{42}$ NPs assembled on a graphene surface to give G-$Fe_{58}Pt_{42}$ NPs, and C) G-$Fe_{58}Pt_{42}$ NPs after acetic acid wash, resulting in G-$Fe_{22}Pt_{78}$ NPs. D) Polarization curves for the ORR in O_2-saturated $HClO_4$ solution (0.1 M) at 295 K. E) Comparison of ORR specific activities of G-$Fe_{22}Pt_{78}$ NPs, G-$Fe_{22}Pt_{78}$ NPs annealed at 100°C, and the commercial C-Pt catalyst. F) ORR polarization curves of G-$Fe_{22}Pt_{78}$ NPs before and after 10000 potential sweeps between 0.4 V and 0.8 V. Adapted from Ref. [91] with permission by the American Chemical Society.

6.2. Molecular Engineering of NP Catalyst Surfaces

ORR activity can be further improved by engineering the coating of the NP catalysts. Ionic liquids (ILs), salts in the liquid state, have been found to be a promising coating material owing to their high conductivity, chemical/thermal stability, wide electrochemical window, and good O_2 solubility.[92] NPs coated with ILs have been shown to reduce the overpotentials of various electrochemical reactions,[93,94] and the coating has been applied to engineer MPt alloys to enhance ORR performance, as demonstrated by nanoporous NiPt impregnated with an IL for the ORR.[95] The nanoporous (np) NiPt alloy (np-NiPt) was prepared through the selective electrochemical dealloying of Ni from the bulk NiPt alloy at 2.1 V (vs. RHE) in a $NiSO_4$ solution (0.05 M). IL-[7-methyl-1,5,7-triazabicyclo[4.4.0]dec-5-ene] [bis(perfluoroethylsulfonyl)imide] [MTBD][beti] (Figure 15A) was dropped onto the dried np-NiPt disc to enable capillary forces to pull the IL into the pores. In the IL structure, the combination of electron donor and acceptor units makes the structure more conductive and affinitive to O_2. Figure 15B shows the ORR polarization curve of the np-NiPt and np-NiPt+[MTBD][beti] in O_2-saturated $HClO_4$ solution (0.1 M). The ORR half-wave potential on the np-NiPt electrode is at 0.96 V (vs. RHE), but once integrated with [MTBD][beti], this half-wave potential shifts positively by 40 mV to 1.0 V, and still maintains the same diffusion-limited current density. Figure 15C compares the specific activities of np-NiPt, np-NiPt+[MTBD][beti] and the single crystal Pt-skin catalyst ($NiPt_3$). The specific activity of np-NiPt+[MTBD][beti] catalyst rises to 18.2 mA cm^{-2} at 0.9 V, which is equal to the best ORR performance on a $NiPt_3$(111) surface.

7. Non-Pt Catalysts for ORR

7.1. M-N-C Catalysts for ORR

Catalysts containing no precious Pt have been highly sought for ORR.[96] Pyrolyzation of the N-containing hydrocarbon complex of Fe or Co yielded a M-*N*-C (M = Fe or Co) composite with some promising ORR activities, but dismal stability.[97,98] Significant progress was made in the catalyst containing a cobalt–polypyrrole complex. In the synthesis, $Co(NO_3)_2{\cdot}6H_2O$ was entrapped into the polypyrrole matrix and reduced with $NaBH_4$ on a carbon support (Vulcan XC 72). Figure 16 shows the cobalt-polypyrrole-carbon composite catalyst with Co coordinated by polypyrrole through its nitrogen binding site.[99] This catalyst was capable of combining high ORR activity with good performance durability and enabled a H_2–O_2 fuel cell to reach a power density of about 0.15 W cm^{-2} with no signs of performance degradation over more than 100 h. However, compared with the Pt-based catalysts, this catalyst still shows an overpotential of 0.15–0.20 V for the ORR. To further improve the ORR activity of Co-*N*-C or Fe-*N*-C composite catalysts, various polymeric

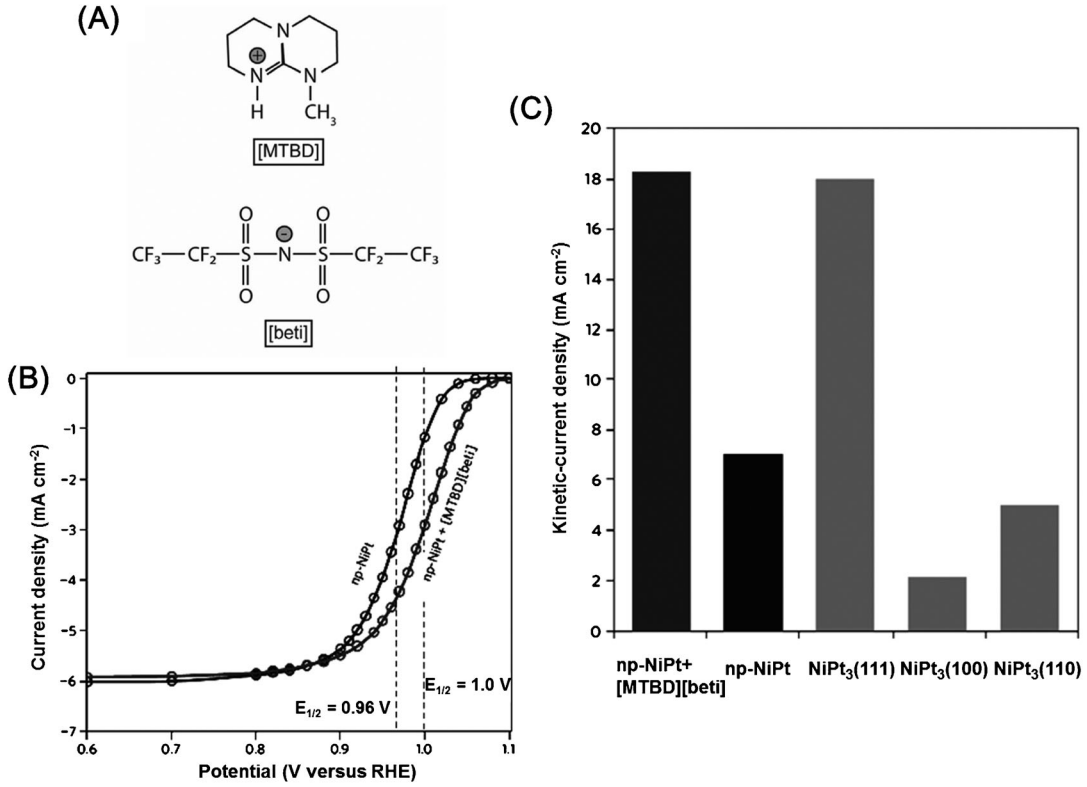

Figure 15. A) The molecular structure of IL-[MTBD][beti]. B) ORR polarization curves of np-NiPt and np-NiPt + [MTBD][beti] in O_2-saturated $HClO_4$ solution (0.1 M) at 25 °C. C) Comparison of specific activities of np-NiPt, np-NiPt + [MTBD][beti], and the low-index crystalline facets of $NiPt_3$ at 0.9 V (vs. RHE) in O_2-saturated $HClO_4$ solution (0.1 M). Adapted from Ref. [95] with permission by the Nature Publishing Group.

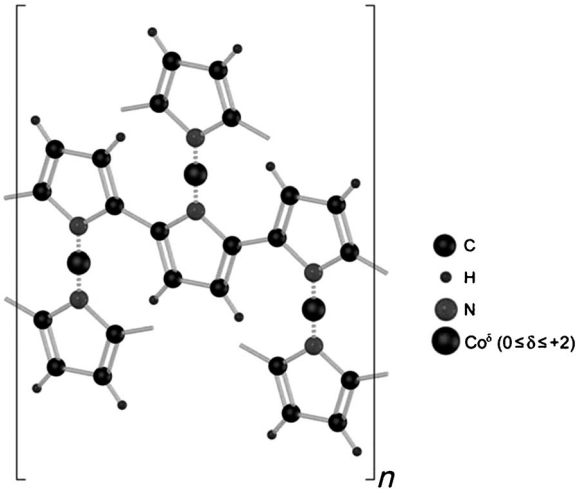

Figure 16. The Co-polypyrrole catalyst as a non-Pt catalyst for the ORR. Adapted from Ref. [99] with permission by the Nature Publishing Group.

precursors have been tested to combine with Fe or Co salts. For example, polyaniline was mixed with ammonium peroxydisulfate, $FeCl_3$, and a carbon support, then pyrolyzed at 900 °C in nitrogen gas for 1 h to give an Fe-*N*-C catalyst that catalyzed the ORR at potentials within ca. 60 mV of the state-of-the-art Pt with a remarkable stability (700 h).[100] Despite these efforts, the chemical nature of the active ORR catalytic sites is not well understood. As a result, the ORR performance of these M-*N*-C catalysts can only be empirically determined by the type of N-containing molecules and transition metals used, and thus are difficult to tune.

7.2. Non-Pt NPs Supported on Carbon Nanomaterials for Enhanced ORR

Carbon nanomaterials, such as nitrogen-doped carbon nanotubes (CNTs),[101] graphene,[102] porous carbon,[103] carbon nanocapsules[104] and CNT composite fibers,[105] as well as iodine-,[106] sulfur-,[107] phosphorus-,[108] and boron-doped carbon[109,110] were also found to be active for ORR. Their activities could be further improved by combining them with metal oxide or sulfide NPs.[111–115] This is demonstrated by depositing Co_3O_4 NPs on N-doped graphene (NG) for improved ORR in alkaline solutions.[111] As shown in Figure 17A, the NG-Co_3O_4 NPs were made by first growing Co_3O_4 NPs on graphene oxide (GO) at 80 °C and then by partially reducing graphene oxide and doping graphene with nitrogen under hydrothermal conditions at 150 °C in an ethanol/water/NH_4OH mixture of. CVs (Figure 17B) and ORR polarization curves (Figure 17C) showed that the NG-Co_3O_4 NPs had a more positive ORR peak potential and a higher peak current than the G-Co_3O_4 NPs, but a more negative peak potential than the C-Pt NPs. This indicates that N-doping assists in a stronger coupling between Co_3O_4 and graphene in NG-Co_3O_4 than in G-Co_3O_4, which leads to higher activity in alkaline solution. Moreover, calculation from Koutecky–Levich plots gave an electron transfer number of 3.9 over a potential range of 0.60–0.75 V, thus indicating that the ORR catalyzed by NG-Co_3O_4 was a $4e^-$ process. The NG-Co_3O_4 catalyst had much better stability for the ORR than the C-Pt catalyst in KOH solution (0.1 M) with an ORR activity almost unchanged over 25000 s of continuous operation (Figure 17D). Once Mn was doped into Co_3O_4, to form NG-$MnCo_2O_4$, the composite catalyst was even more active for ORR.[112] Its ORR peak potential was 0.88 V (vs. RHE), which was ca. 20 mV more positive than that of the G-Co_3O_4 catalyst and only ca. 20 mV more negative than that of the C-Pt catalyst. Similarly, G-$Co_{1-x}S$,[113] mesoporous carbon-MnO,[114] G-CuO NPs,[115] and even G-NG quantum dots[116] have been synthesized and studied for ORR catalysis in KOH solutions.

In the above G-NP catalyst systems, the NPs are deposited directly onto the graphene surface by in situ chemical deposition. Through such deposition techniques, it is difficult to control NP sizes, morphologies, and G-NP interactions.

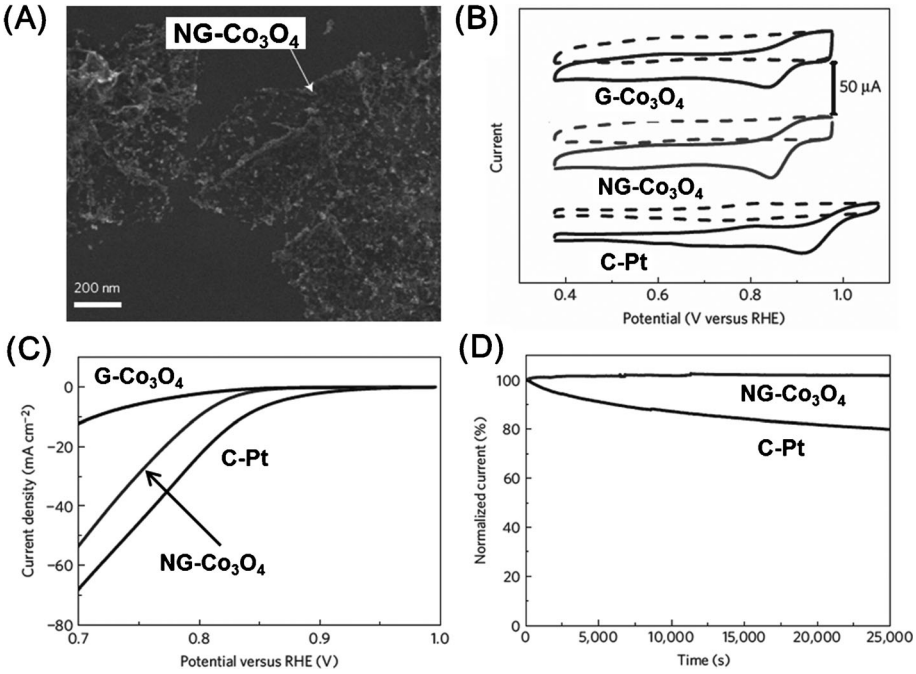

Figure 17. A) SEM image of the NG-Co_3O_4 hybrid. B) CV curves of G-Co_3O_4, NG-Co_3O_4, and C-Pt on GC electrodes in O_2-saturated (——) or Ar-saturated 0.1 M KOH solution (-----). C) ORR polarization curves of G-Co_3O_4, NG-Co_3O_4, and C-Pt in O_2-saturated KOH solution (0.1 M). D) Chronoamperometric responses (percentage of current retained vs. operation time) of the NG-Co_3O_4 hybrid and C-Pt on carbon fiber paper electrodes kept at 0.70 V (vs. RHE) in O_2-saturated KOH solution (0.1 M). Adapted from Ref. [111] with permission by the Nature Publishing Group.

This problem can be solved by the self-assembly method described for the synthesis of the G-FePt NP catalyst.[91] In this demonstration, monodisperse core–shell Co/CoO NPs were synthesized and then deposited on the graphene surface by solution-phase self-assembly.[117] Figure 18A and B shows typical TEM images of the 10 nm Co/CoO NPs (8 nm Co core plus 1 nm CoO shell) and the composite G-Co/CoO NPs. G-Co/CoO was an active electrocatalyst for ORR. Figure 18C shows the ORR polarization curves of graphene, C-Co/CoO, and G-Co/CoO catalysts in KOH solution (0.1M). The G-Co/CoO NPs have a more positive half-wave potential (−0.176 V) for ORR than the C-Co/CoO NPs (−0.290 V), and much more positive than that of graphene, indicating that graphene as a support indeed provides a significant enhancement in Co/CoO catalysis for the ORR. The ORR activity of the G-Co/CoO NPs could be further controlled by the dimensions of Co and CoO, and core–shell NPs with a larger Co core and a thinner CoO shell showed higher activity (Figure 18D). The ORR activity of the G-Co/CoO NP catalyst (8 nm Co core and 1 nm CoO shell) was comparable with the commercial C-Pt catalyst in O_2-saturated KOH solution (0.1M; Figure 18E). There is only a 25 mV difference in half-wave potentials between the ORR polarization curves from the G-Co/CoO and the C-Pt NP catalysts. The G-Co/Co NPs have a steeper polarization curve and a higher current density than the C-Pt NPs near the diffusion limit region. The observed ORR activity of G-Co/CoO decreased more slowly than that of C-Pt after a 20 h stability test (Figure 18F), thus indicating the greater stability of G-Co/CoO in KOH solution.

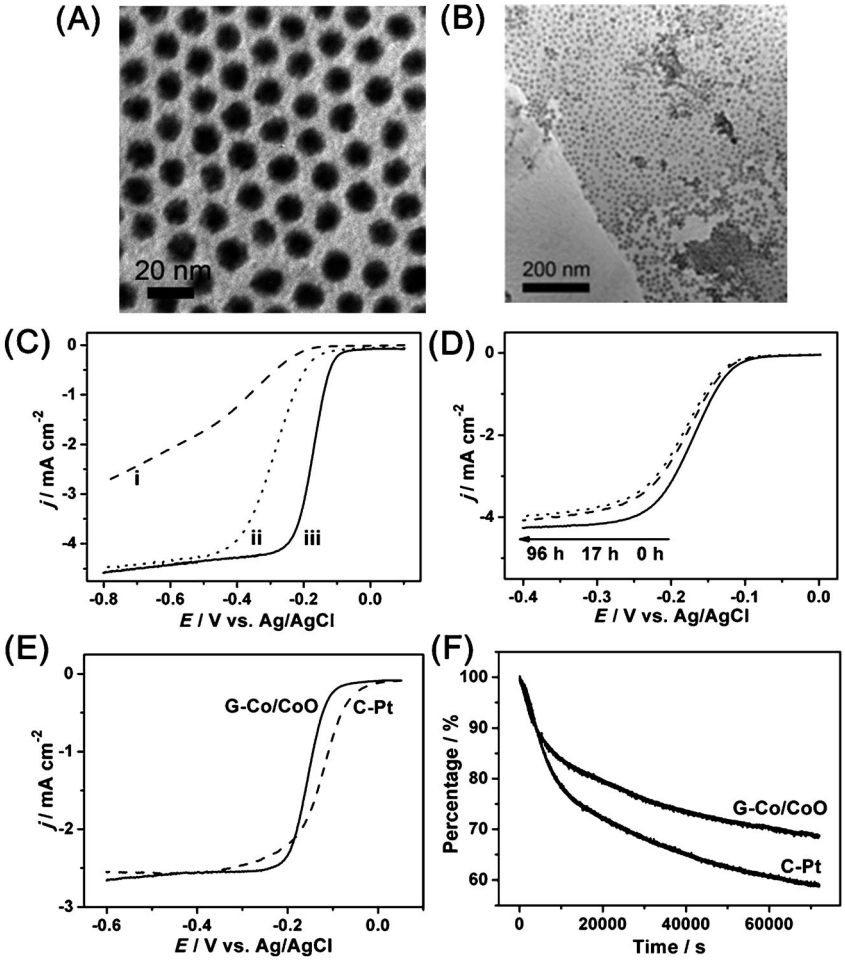

Figure 18. TEM images of A) Co/CoO and B) G-Co/CoO NPs. C) ORR polarization curves of graphene (i), C-Co/CoO NPs (ii) and G-Co/CoO NPs (iii). D) ORR polarization curves of G-Co/CoO NPs after heating at 70°C in air for 0 h, 17 h, and 96 h, which leads to an increase in CoO shell thickness from 1 nm to 3 nm. E) ORR polarization curves of G-Co/CoO NPs and the commercial C-Pt catalyst. F) Chronoamperometric responses for ORR from the G-Co/CoO NPs and the commercial C-Pt at −0.3 V. Adapted from Ref. [117].

7.3. Non-Metal Nanocatalysts for ORR

Although the G-NP catalysts show some great potential for enhancing ORR activity and stability in alkaline solution, their ORR performance in acidic solutions is very poor. Recently a new non-metal system, N-doped CNT-G (NT-G), was introduced as an advanced nanocatalyst for ORR in acidic media.[118] To make this kind of complex, multi-walled (2–3 walled) CNTs were oxidized in $KMnO_4/H_2SO_4$ at 65°C to partially unzip the outer walls. Then, the oxidized composite, including CNTs and GO, was annealed under NH_3 at 900°C to give the NT-G composite. Figure 19A is a typical aberration-corrected TEM image of the NT-G composite. The CNTs are mostly 2–3 walled, with their outer walls damaged and exfoliated to form graphene- or ribbon-like structures. Figure 19B shows the ORR polarization curves of the NT-G and commercial Pt catalysts in O_2-saturated $HClO_4$ solution (0.1M). Although the NT-G is still not as active as Pt, its polarization curve does show a well-defined plateau that relates to a diffusion-limiting current. In KOH solution (0.1M), the NT-G catalyst performed equally well, with the ORR activity approaching that of the Pt catalyst (Figure 19C). The durability of the CNT-G catalyst was estimated by cycling the catalysts between 0.6 V and 1.0 V at 50 mV s^{-1} in O_2-saturated $HClO_4$ solution (0.1M). After 8000 cycles, the $E_{1/2}$ negatively shifted only 17 mV (Figure 19D), which indicates that the catalyst is reasonably stable.

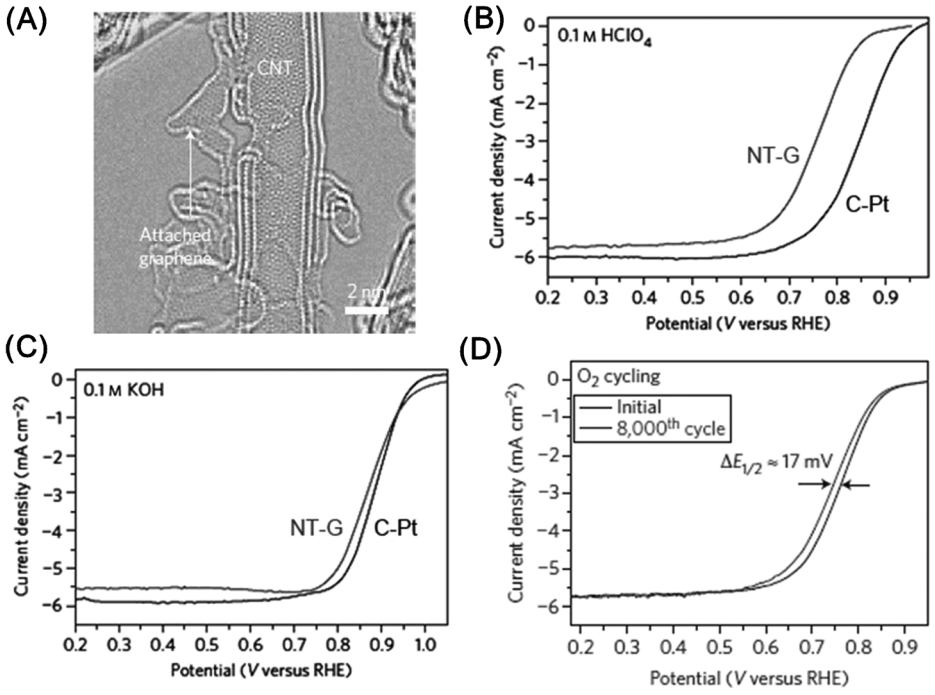

Figure 19. A) Aberration-corrected TEM image of the NT-G composite, showing damaged outer walls and exfoliated graphene pieces attached to double- or triple-walled CNTs. B, C) ORR polarization curves of C-Pt and NT-G in O_2-saturated solutions of $HClO_4$ (0.1 M; B) and KOH (0.1 M; C) solution. D) ORR polarization curves of the NT-G catalyst before and after 8000 potential cycles between 0.6 V and 1.0 V (vs. RHE) in O_2-saturated $HClO_4$ solution (0.1 M). Adapted from Ref. [118] with permission by the Nature Publishing Group.

8. Summary and Outlook

Efforts in searching for efficient NP catalysts for ORR have led to the formation of various kinds of NPs with precise control of NP size, shape, composition, and structure. Such monodisperse NPs allow, for the first time, detailed studies of the ORR on the surface of the catalyst.

For monodisperse Pt NPs, their ORR catalysis is often tuned by NP shapes, with octahedral (or tetrahedral) NPs being more active in $HClO_4$, and cubic NPs being more active in H_2SO_4. For MPt alloy NPs, although their shape effect on the ORR is similar to that of the Pt NPs, their composition often plays a more important role in tuning ORR catalysis. To further improve ORR activity and durability, core–shell NPs have been introduced, where Pt (or MPt) is deposited on other MPt or non-Pt metal NP cores. In this core–shell structure, both electronic (alloying) and strain (geometric) effects can be tuned by the core NPs and shell thickness to maximize ORR efficiency; core–shell NPs with thin shells (ca. 1 nm or thinner) were found to be the most active and durable catalysts for the ORR. Recent studies on support and coating effects on NP catalysis also led to the development of a new graphene support and an IL coating that are further capable of improving ORR catalysis, owing to controlled G-NP interactions and enhanced O_2-affinity on the NP surface. These seem to indicate that G-core–shell NPs coated with ILs should be the most robust catalysts for ORR.

In an effort to develop non-Pt catalysts for ORR, NG-NPs, NG-carbon nanomaterials, and M-*N*-C (M = Fe, Co) composite complexes have been extensively explored. New syntheses capable of tuning catalyst parameters should provide some promising solutions for the future development of non-Pt catalysts for fuel cells and other energy-device applications.

Despite the exciting progress made in the past decade, there are still some serious challenges ahead in developing practical catalysts for the ORR. There is still no gold-standard catalyst for the ORR, to which all newly reported NP catalysts can be compared; such a standard would allow researchers to determine the most important factor(s) for comparing NP activity and stability. In particular, the durability of the majority of the existing Pt-based catalysts is still far from satisfying. Pt or MPt-alloy NPs are only good for model studies because of the heavy use of Pt in the NP components. Core–shell NPs reduce Pt usage and their ORR catalysis can be tuned through both electronic and strain effects to achieve high activity and durability that can be further improved by using graphene as a support and ILs as coating materials. However, core–shell NP synthesis is new, and core–shell morphology control is not as well developed as for Pt or MPt alloy NPs. Graphene and ILs cannot be readily synthesized, and without simplifying the preparation steps, their potential for commercial applications is very limited.

Non-Pt catalysts have also attracted much attention. Recent NG-M oxide (MO) NPs, M-*N*-C and CNT-NG, provide some exciting new materials for ORR studies. At present, non-Pt NG-MO NPs are mostly used in alkaline solution; M-*N*-C or CNT-NG can be used in acidic solution, but it is not very clear what makes these catalysts active, and therefore it is still impossible to tune ORR catalysis.

Despite these challenges, recent experimental and computational work does provide researchers with much desired information for understanding catalyst design and synthesis. The work further hints that Pt is thus far the best catalyst component for the ORR, and that future design and synthesis should aim to minimize Pt usage without sacrificing much ORR catalytic efficiency. Developing non-Pt catalysts with Pt-equivalent ORR efficiency is certainly exciting. These non-Pt catalysts may be a new type of core–shell NPs, a new form of composite NPs or carbon-based nanomaterials, or even a well-designed M-*N*-C complex network. No matter what catalyst will come out as a winner, in the long run the chemical principles developed will surely direct us in our future endeavors towards the rational design and synthesis of

nanocatalysts for the ORR and many other chemical reactions.

Work at Brown University was supported in part by the U.S. Department of Energy, Office of Energy Efficiency and Renewable Energy, the Fuel Cell Technologies Program, and by the U.S. Army Research Laboratory and the U.S. Army Research Office under the Multi University Research Initiative MURI (W911NF-11-1-0353) on "Stress-Controlled Catalysis via Engineered Nanostructures".

Received: September 5, 2012
Published online: June 14, 2013

[1] R. Borup, J. Meyers, B. Pivovar, Y. S. Kim, R. Mukundan, N. Garland, D. Myers, M. Wilson, F. Garzon, D. Wood, P. Zelenay, K. More, K. Stroh, T. Zawodzinski, J. Boncella, J. E. McGrath, M. Inaba, K. Miyatake, M. Hori, K. Ota, Z. Ogumi, S. Miyata, A. Nishikata, Z. Siroma, Y. Uchimoto, K. Yasuda, K. Kimijima, N. Iwashita, *Chem. Rev.* **2007**, *107*, 3904 – 3951.

[2] Y.-J. Wang, D. P. Wilkinson, J. Zhang, *Chem. Rev.* **2011**, *111*, 7625 – 7651.

[3] Z. Chen, D. Higgins, A. Yu, L. Zhang, J. Zhang, *Energy Environ. Sci.* **2011**, *4*, 3167 – 3192.

[4] Y. Bing, H. Liu, L. Zhang, D. Ghosh, J. Zhang, *Chem. Soc. Rev.* **2010**, *39*, 2184 – 2202.

[5] D. S. Su, G. Sun, *Angew. Chem.* **2011**, *123*, 11774 – 11777; *Angew. Chem. Int. Ed.* **2011**, *50*, 11570 – 11572.

[6] J. Chen, B. Lim, E. P. Lee, Y. Xia, *Nano Today* **2009**, *4*, 81 – 95.

[7] S. Guo, E. Wang, *Nano Today* **2011**, *6*, 240 – 264.

[8] Z. Chen, M. Waje, W. Li, Y. Yan, *Angew. Chem.* **2007**, *119*, 4138 – 4141; *Angew. Chem. Int. Ed.* **2007**, *46*, 4060 – 4063.

[9] C. Koenigsmann, A. C. Santulli, K. Gong, M. B. Vukmirovic, W.-P. Zhou, E. Sutter, S. S. Wong, R. R. Adzic, *J. Am. Chem. Soc.* **2011**, *133*, 9783 – 9795.

[10] C. Koenigsmann, E. Sutter, T. A. Chiesa, R. R. Adzic, S. S. Wong, *Nano Lett.* **2012**, *12*, 2013 – 2020.

[11] C. Koenigsmann, E. Sutter, R. R. Adzic, S. S. Wong, *J. Phys. Chem. C* **2012**, *116*, 15297 – 15306.

[12] S. Sun, G. Zhang, D. Geng, Y. Chen, R. Li, M. Cai, X. Sun, *Angew. Chem.* **2011**, *123*, 442 – 446; *Angew. Chem. Int. Ed.* **2011**, *50*, 422 – 426.

[13] U.S.D.O. Energy, http://www1.eere.energy.gov/hydrogenandfuelcells/mypp/pdfs/fuel_cells.pdf.

[14] a) M. R. Tarasevich, A. Sadkowski, E. Yeager, *Comprehensive Treatise of Electrochemistry, Vol. 7* (Eds.: B. E. Conway, J. O. Bockris, E. B. Yeager, R. E. White), Plenum, New York, **1983**, pp. 301; b) D. Yu, E. Nagelli, F. Du, L. Dai, *J. Phys. Chem. Lett.* **2010**, *1*, 2165 – 2173; c) J. Zhang, K. Sasaki, E. Sutter, R. R. Adzic, *Science* **2007**, *315*, 220 – 222.

[15] Y. Zheng, Y. Jiao, M. Jaroniec, Y. Jin, S. Z. Qiao, *Small* **2012**, *8*, 3550 – 3566.

[16] J. K. Nørskov, J. Rossmeisl, A. Logadottir, L. Lindqvist, J. R. Kitchin, T. Bligaard, H. Jónsson, *J. Phys. Chem. B* **2004**, *108*, 17886 – 17892.

[17] H. A. Gasteiger, S. S. Kocha, B. Sompalli, F. T. Wagner, *Appl. Catal. B* **2005**, *56*, 9 – 35.

[18] "Rotating thin-film method for supported catalysts": T. J. Schmidt, H. A. Gasteiger, *Handbook of Fuel Cells-Fundamentals, Technology and Applications, Vol. 2* (Eds.: W. Vielstich, H. Gasteiger, A. Lamm), John Wiley & Sons, New York, **2003**, pp. 316 – 333.

[19] F. Gloaguen, P. Convert, S. Gamburzev, O. A. Velev, S. Srinivasan, *Electrochim. Acta* **1998**, *43*, 3767 – 3772.

[20] J. Perez, E. R. Gonzalez, E. A. Ticianelli, *Electrochim. Acta* **1998**, *44*, 1329 – 1339.

[21] B. Lim, M. Jiang, P. H. C. Camargo, E. C. Cho, J. Tao, X. Lu, Y. Zhu, Y. Xia, *Science* **2009**, *324*, 1302 – 1305.

[22] T. J. Schmidt, H. A. Gasteiger, G. D. Stäb, P. M. Urban, D. M. Kolb, R. J. Behm, *J. Electrochem. Soc.* **1998**, *145*, 2354 – 2358.

[23] S. Wang, D. Yu, L. Dai, *J. Am. Chem. Soc.* **2011**, *133*, 5182 – 5185.

[24] S. Wang, D. Yu, L. Dai, D. W. Chang, J.-B. Baek, *ACS Nano* **2011**, *5*, 6202 – 6209.

[25] a) M. L. Sattler, P. N. Ross, *Ultramicroscopy* **1986**, *20*, 21 – 28; b) K. J. Kinoshita, *J. Electrochem. Soc.* **1990**, *137*, 845 – 848.

[26] V. Mazumder, Y. Lee, S. Sun, *Adv. Funct. Mater.* **2010**, *20*, 1224 – 1231.

[27] Y. Xia, Y. Xiong, B. Lim, S. E. Skrabalak, *Angew. Chem.* **2008**, *121*, 62 – 108; *Angew. Chem. Int. Ed.* **2008**, *48*, 60 – 103.

[28] a) T. S. Ahmadi, Z. L. Wang, T. C. Green, A. Henglein, M. A. El-Sayed, *Science* **1996**, *272*, 1924 – 1926; b) J. M. Petroski, Z. L. Wang, T. C. Green, M. A. El-Sayed, *J. Phys. Chem. B* **1998**, *102*, 3316 – 3320.

[29] C. Wang, H. Daimon, T. Onodera, T. Koda, S. Sun, *Angew. Chem.* **2008**, *120*, 3644 – 3647; *Angew. Chem. Int. Ed.* **2008**, *47*, 3588 – 3591.

[30] C. Wang, H. Daimon, Y. Lee, J. Kim, S. Sun, *J. Am. Chem. Soc.* **2007**, *129*, 6974 – 6975.

[31] N. Tian, Z.-Y. Zhou, S.-G. Sun, Y. Ding, Z. L. Wang, *Science* **2007**, *316*, 732 – 735.

[32] T. Yu, D. Y. Kim, H. Zhang, Y. Xia, *Angew. Chem.* **2011**, *123*, 2825 – 2829; *Angew. Chem. Int. Ed.* **2011**, *50*, 2773 – 2777.

[33] B. Lim, X. Lu, M. Jiang, P. H. C. Camargo, E. C. Cho, E. P. Lee, Y. Xia, *Nano Lett.* **2008**, *8*, 4043 – 4047.

[34] V. R. Stamenkovic, B. Fowler, B. S. Mun, G. F. Wang, P. N. Ross, C. A. Lucas, N. M. Markovic, *Science* **2007**, *315*, 493 – 497.

[35] a) C. Wang, N. M. Markovic, V. R. Stamenkovic, *ACS Catal.* **2012**, *2*, 891 – 898; b) J. Greeley, I. E. L. Stephens, A. S. Bondarenko, T. P. Johansson, H. A. Hansen, T. F. Jaramillo, J. Rossmeisl, I. Chorkendorff, J. K. Nørskov, *Nat. Chem.* **2009**, *1*, 552 – 556.

[36] V. R. Stamenkovic, B. S. Mun, M. Arenz, K. J. J. Mayrhofer, C. A. Lucas, G. F. Wang, P. N. Ross, N. M. Markovic, *Nat. Mater.* **2007**, *6*, 241 – 247.

[37] a) S. H. Sun, C. B. Murray, D. Weller, L. Folks, A. Moser, *Science* **2000**, *287*, 1989 – 1992; b) M. Chen, J. Kim, J. P. Liu, H. Y. Fan, S. H. Sun, *J. Am. Chem. Soc.* **2006**, *128*, 7132 – 7133; c) S. Sun, S. Anders, T. Thomson, J. E. E. Baglin, M. F. Toney, H. F. Hamann, C. B. Murray, B. D. Terris, *J. Phys. Chem. B* **2003**, *107*, 5419 – 5425; d) C. Liu, X. Wu, T. Klemmer, N. Shukla, X. Yang, D. Weller, *J. Phys. Chem. B* **2004**, *108*, 6121; e) S. H. Sun, *Adv. Mater.* **2006**, *18*, 393 – 403; f) J. Kim, C. Rong, J. P. Liu, S. Sun, *Adv. Mater.* **2009**, *21*, 906 – 909; g) C. Xu, Z. Yuan, N. Kohler, J. Kim, M. A. Chung, S. Sun, *J. Am. Chem. Soc.* **2009**, *131*, 15346 – 15351; h) S. Guo, S. Zhang, X. Sun, S. Sun, *J. Am. Chem. Soc.* **2011**, *133*, 15354 – 15357; i) S. Zhang, S. Guo, H. Zhu, D. Su, S. Sun, *J. Am. Chem. Soc.* **2012**, *134*, 5060 – 5063.

[38] See Ref. [27].

[39] a) E. V. Shevchenko, D. V. Talapin, H. Schnablegger, A. Kornowski, O. Festin, P. Svedlindh, M. Haase, H. Weller, *J. Am. Chem. Soc.* **2003**, *125*, 9090 – 9101; b) J.-I. Park, J. Cheon, *J. Am. Chem. Soc.* **2001**, *123*, 5743 – 5746.

[40] a) K. Ono, R. Okuda, Y. Ishii, S. Kamimura, M. Oshima, *J. Phys. Chem. B* **2003**, *107*, 1941 – 1942; b) D. C. Lee, A. Ghezelbash, C. A. Stowell, B. A. Korgel, *J. Phys. Chem. B* **2006**, *110*, 20906 – 20911; c) D. C. Lee, D. K. Smith, A. T. Heitsch, B. A. Korgel, *Annu. Rep. Prog. Chem. Sect. C* **2007**, *103*, 351 – 402; d) Y. Kang, C. B. Murray, *J. Am. Chem. Soc.* **2010**, *132*, 7568 – 7569.

[41] Y. Liu, D. Li, S. Sun, *J. Mater. Chem.* **2011**, *21*, 12579 – 12587.
[42] a) J. Wu, A. Gross, H. Yang, *Nano Lett.* **2011**, *11*, 798 – 802; b) J. Zhang, J. Fang, *J. Am. Chem. Soc.* **2009**, *131*, 18543 – 18547; c) J. Zhang, H. Yang, J. Fang, S. Zou, *Nano Lett.* **2010**, *10*, 638 – 644; d) D. Xu, S. Bliznakov, Z. Liu, J. Fang, N. Dimitrov, *Angew. Chem.* **2010**, *122*, 1304 – 1307; *Angew. Chem. Int. Ed.* **2010**, *49*, 1282 – 1285; e) D. Xu, Z. Liu, H. Yang, Q. Liu, J. Zhang, J. Fang, S. Zou, K. Sun, *Angew. Chem.* **2009**, *121*, 4281 – 4285; *Angew. Chem. Int. Ed.* **2009**, *48*, 4217 – 4221; f) H. Yang, J. Zhang, K. Sun, S. Zou, J. Fang, *Angew. Chem.* **2010**, *122*, 7000 – 7003; *Angew. Chem. Int. Ed.* **2010**, *49*, 6848 – 6851.
[43] a) F. J. Perez-Alonso, D. N. McCarthy, A. Nierhoff, P. Hernandez-Fernandez, C. Strebel, I. E. L. Stephens, J. H. Nielsen, I. Chorkendorff, *Angew. Chem.* **2012**, *124*, 4719 – 4721; *Angew. Chem. Int. Ed.* **2012**, *51*, 4641 – 4643; b) I. N. Leontyev, S. V. Belenov, V. E. Guterman, P. Haghi-Ashtiani, A. P. Shaganov, B. Dkhil, *J. Phys. Chem. C* **2011**, *115*, 5429 – 5434.
[44] C. Wang, D. van der Vliet, K.-C. Chang, H. You, D. Strmcnik, J. A. Schlueter, N. M. Markovic, V. R. Stamenkovic, *J. Phys. Chem. C* **2009**, *113*, 19365 – 19368.
[45] C. Wang, G. Wang, D. van der Vliet, K.-C. Chang, N. M. Markovica, V. R. Stamenkovic, *Phys. Chem. Chem. Phys.* **2010**, *12*, 6933 – 6939.
[46] C. Wang, M. Chi, D. Li, D. van der Vliet, G. Wang, Q. Lin, J. F. Mitchell, K. L. More, N. M. Markovic, V. R. Stamenkovic, *ACS Catal.* **2011**, *1*, 1355 – 1359.
[47] W. Chen, J. Kim, S. Sun, S. Chen, *J. Phys. Chem. C* **2008**, *112*, 3891 – 3898.
[48] C. Wang, M. Chi, G. Wang, D. van der Vliet, D. Li, K. More, H.-H. Wang, J. A. Schlueter, N. M. Markovic, V. R. Stamenkovic, *Adv. Funct. Mater.* **2011**, *21*, 147 – 152.
[49] M. K. Carpenter, T. E. Moylan, R. S. Kukreja, M. H. Atwan, M. M. Tessema, *J. Am. Chem. Soc.* **2012**, *134*, 8535 – 8542.
[50] a) Y. Wu, S. Cai, D. Wang, W. He, Y. Li, *J. Am. Chem. Soc.* **2012**, *134*, 8975 – 8981; b) C. Cui, L. Gan, H.-H. Li, S.-H. Yu, M. Heggen, P. Strasser, *Nano Lett.* **2012**, *12*, 5885 – 5889.
[51] See Ref. [42c].
[52] J. Wu, J. Zhang, Z. Peng, S. Yang, F. T. Wagner, H. Yang, *J. Am. Chem. Soc.* **2010**, *132*, 4984 – 4985.
[53] J. Wu, L. Qi, H. You, A. Gross, J. Li, H. Yang, *J. Am. Chem. Soc.* **2012**, *134*, 11880 – 11883.
[54] V. R. Stamenkovic, B. S. Mun, K. J. J. Mayrhofer, P. N. Ross, N. M. Markovic, *J. Am. Chem. Soc.* **2006**, *128*, 8813 – 8819.
[55] V. Stamenkovic, B. S. Mun, K. J. J. Mayrhofer, P. N. Ross, N. M. Markovic, J. Rossmeisl, J. Greeley, J. K. Norskov, *Angew. Chem.* **2006**, *118*, 2963 – 2967; *Angew. Chem. Int. Ed.* **2006**, *45*, 2897 – 2901.
[56] J. Kim, Y. Lee, S. Sun, *J. Am. Chem. Soc.* **2010**, *132*, 4996 – 4997.
[57] J. Zhang, Y. Mo, M. B. Vukmirovic, R. Klie, K. Sasaki, R. R. Adzic, *J. Phys. Chem. B* **2004**, *108*, 10955 – 10964.
[58] K. Sasaki, H. Naohara, Y. Cai, Y. M. Choi, P. Liu, M. B. Vukmirovic, J. X. Wang, R. R. Adzic, *Angew. Chem.* **2010**, *122*, 8784 – 8789; *Angew. Chem. Int. Ed.* **2010**, *49*, 8602 – 8607.
[59] a) W.-P. Zhou, K. Sasaki, D. Su, Y. Zhu, J. X. Wang, R. R. Adzic, *J. Phys. Chem. C* **2010**, *114*, 8950 – 8957; b) J. X. Wang, H. Inada, L. Wu, Y. Zhu, Y. Choi, P. Liu, W.-P. Zhou, R. R. Adzic, *J. Am. Chem. Soc.* **2009**, *131*, 17298 – 17302; c) D. Wang, H. L. Xin, H. Wang, Y. Yu, E. Rus, D. A. Muller, F. J. DiSalvo, H. D. Abruña, *Chem. Mater.* **2012**, *24*, 2274 – 2281.
[60] K. A. Kuttiyiel, K. Sasaki, Y. Choi, D. Su, P. Liu, R. R. Adzic, *Energy Environ. Sci.* **2012**, *5*, 5297 – 5304.
[61] T. Ghosh, M. B. Vukmirovic, F. J. DiSalvo, R. R. Adzic, *J. Am. Chem. Soc.* **2010**, *132*, 906 – 907.
[62] H. I. Karan, K. Sasaki, K. Kuttiyiel, C. A. Farberow, M. Mavrikakis, R. R. Adzic, *ACS Catal.* **2012**, *2*, 817 – 824.
[63] K. Gong, D. Su, R. R. Adzic, *J. Am. Chem. Soc.* **2010**, *132*, 14364 – 14366.
[64] a) J. Zhang, M. B. Vukmirovic, K. Sasaki, A. U. Nilekar, M. Mavrikakis, R. R. Adzic, *J. Am. Chem. Soc.* **2005**, *127*, 12480 – 12481; b) R. R. Adzic, J. Zhang, K. Sasaki, M. B. Vukmirovic, M. Shao, J. X. Wang, A. U. Nilekar, M. Mavrikakis, J. A. Valerio, F. Uribe, *Top. Catal.* **2007**, *46*, 249 – 262.
[65] V. Mazumder, M. Chi, K. L. More, S. Sun, *Angew. Chem.* **2010**, *122*, 9558 – 9562; *Angew. Chem. Int. Ed.* **2010**, *49*, 9368 – 9372.
[66] J. Zhang, Y. Tang, K. Lee, M. Ouyang, *Science* **2010**, *327*, 1634 – 1638.
[67] V. Mazumder, M. Chi, K. L. More, S. Sun, *J. Am. Chem. Soc.* **2010**, *132*, 7848 – 7849.
[68] V. Mazumder, S. Sun, *J. Am. Chem. Soc.* **2009**, *131*, 4588 – 4589.
[69] C. Wang, D. van der Vliet, K. L. More, N. J. Zaluzec, S. Peng, S. Sun, H. Daimon, G. Wang, J. Greeley, J. Pearson, A. P. Paulikas, G. Karapetrov, D. Strmcnik, N. M. Markovic, V. R. Stamenkovic, *Nano Lett.* **2011**, *11*, 919 – 926.
[70] V. Komanicky, K. C. Chang, A. Menzel, N. M. Markovic, H. You, X. Wang, D. Myers, *J. Electrochem. Soc.* **2006**, *153*, B446 – B451.
[71] H. You, D. J. Zurawski, Z. Nagy, R. M. Yonco, *J. Chem. Phys.* **1994**, *100*, 4699 – 4702.
[72] J. Yang, X. Chen, X. Yang, J. Y. Ying, *Energy Environ. Sci.* **2012**, *5*, 8976 – 8981.
[73] P. Strasser, S. Koh, T. Anniyev, J. Greeley, K. More, C. Yu, Z. Liu, S. Kaya, D. Nordlund, H. Ogasawara, M. F. Toney, A. Nilsson, *Nat. Chem.* **2010**, *2*, 454 – 460.
[74] R. Srivastava, P. Mani, N. Hahn, P. Strasser, *Angew. Chem.* **2007**, *119*, 9146 – 9149; *Angew. Chem. Int. Ed.* **2007**, *46*, 8988 – 8991.
[75] S. Koh, P. Strasser, *J. Am. Chem. Soc.* **2007**, *129*, 12624 – 12625.
[76] P. Mani, R. Srivastava, P. Strasser, *J. Power Sources* **2011**, *196*, 666 – 673.
[77] a) C. Wang, M. Chi, D. Li, D. Strmcnik, D. van der Vliet, G. Wang, V. Komanicky, K.-C. Chang, A. P. Paulikas, D. Tripkovic, J. Pearson, K. L. More, N. M. Markovic, V. R. Stamenkovic, *J. Am. Chem. Soc.* **2011**, *133*, 14396 – 14403; b) L. Gan, M. Heggen, S. Rudi, P. Strasser, *Nano Lett.* **2012**, *12*, 5423 – 5430.
[78] K. J. J. Mayrhofer, V. Juhart, K. Hartl, M. Hanzlik, M. Zrenz, *Angew. Chem.* **2009**, *121*, 3581 – 3583; *Angew. Chem. Int. Ed.* **2009**, *48*, 3529 – 3531.
[79] See Ref. [45].
[80] B. N. Wanjala, B. Fang, J. Luo, Y. Chen, J. Yin, M. H. Engelhard, R. Loukrakpam, C.-J. Zhong, *J. Am. Chem. Soc.* **2011**, *133*, 12714 – 12727.
[81] C. Wang, D. Li, M. Chi, J. Pearson, R. B. Rankin, J. Greeley, Z. Duan, G. Wang, D. van der Vliet, K. L. More, N. M. Markovic, V. R. Stamenkovic, *J. Phys. Chem. Lett.* **2012**, *3*, 1668 – 1673.
[82] J. Hou, Y. Shao, M. W. Ellis, R. B. Moored, B. Yi, *Phys. Chem. Chem. Phys.* **2011**, *13*, 15384 – 15402.
[83] a) S. Guo, S. Dong, *Chem. Soc. Rev.* **2011**, *40*, 2644 – 2672; b) S. Guo, S. Dong, E. Wang, *ACS Nano* **2010**, *4*, 547 – 555.
[84] S. Guo, E. Wang, *Acc. Chem. Res.* **2011**, *44*, 491 – 500.
[85] R. Kou, Y. Shao, D. Wang, M. H. Engelhard, J. H. Kwak, J. Wang, V. V. Viswanathan, C. Wang, Y. Lin, Y. Wang, I. A. Aksay, J. Liu, *Electrochem. Commun.* **2009**, *11*, 954 – 957.
[86] Y. Shao, S. Zhang, C. Wang, Z. Nie, J. Liu, Y. Wang, Y. Lin, *J. Power Sources* **2010**, *195*, 4600 – 4605.
[87] Y. Tan, C. Xu, G. Chen, N. Zheng, Q. Xie, *Energy Environ. Sci.* **2012**, *5*, 6923 – 6927.
[88] a) R. Kou, Y. Shao, D. Mei, Z. Nie, D. Wang, C. Wang, V. V. Viswanathan, S. Park, I. A. Aksay, Y. Lin, Y. Wang, J. Liu, *J. Am. Chem. Soc.* **2011**, *133*, 2541 – 2547; b) Y. Li, Y. Li, E. Zhu, T. McLouth, C.-Y. Chiu, X. Huang, Y. Huang, *J. Am. Chem. Soc.* **2012**, *134*, 12326 – 12329.
[89] B. P. Vinayan, R. Nagar, N. Rajalakshmi, S. Ramaprabhu, *Adv. Funct. Mater.* **2012**, *22*, 3519 – 3526.

[90] C. V. Rao, A. Lee, M. Reddy, Y. Ishikawa, P. M. Ajayan, *Carbon* **2011**, *49*, 931 – 936.
[91] S. Guo, S. Sun, *J. Am. Chem. Soc.* **2012**, *134*, 2492 – 2495.
[92] a) Y. Zhang, Y. Shen, J. Yuan, D. Han, Z. Wang, Q. Zhang, L. Niu, *Angew. Chem.* **2006**, *118*, 5999 – 6002; *Angew. Chem. Int. Ed.* **2006**, *45*, 5867 – 5870; b) Y. F. Shen, Y. J. Zhang, Q. X. Zhang, L. Niu, T. Y. You, A. Ivaska, *Chem. Commun.* **2005**, 4193 – 4195.
[93] a) S. Guo, S. Dong, E. Wang, *Adv. Mater.* **2010**, *22*, 1269 – 1272; b) S. Guo, D. Wen, Y. Zhai, S. Dong, E. Wang, *Biosens. Bioelectron.* **2011**, *26*, 3475 – 3481.
[94] a) C. S. Shan, H. F. Yang, J. F. Song, D. X. Han, A. Ivaska, L. Niu, *Anal. Chem.* **2009**, *81*, 2378 – 2382; b) Z. J. Wang, Q. X. Zhang, D. Kuehner, A. Ivaska, L. Niu, *Green Chem.* **2008**, *10*, 907 – 909; c) Z. Wang, Q. Zhang, D. Kuehner, X. Xu, A. Ivaska, L. Niu, *Carbon* **2008**, *46*, 1687 – 1692; d) B. Wu, D. Hu, Y. Kuang, B. Liu, X. Zhang, J. Chen, *Angew. Chem.* **2009**, *121*, 4845 – 4848; *Angew. Chem. Int. Ed.* **2009**, *48*, 4751 – 4754.
[95] J. Snyder, T. Fujita, M. W. Chen, J. Erlebacher, *Nat. Mater.* **2010**, *9*, 904 – 907.
[96] F. Jaouen, E. Proietti, M. Lefevre, R. Chenitz, J.-P. Dodelet, G. Wu, H. T. Chung, C. M. Johnston, P. Zelenay, *Energy Environ. Sci.* **2011**, *4*, 114 – 130.
[97] R. Jasinski, *Nature* **1964**, *201*, 1212 – 1213.
[98] H. Jahnke, M. Schonborn, G. Zimmermann, *Top. Curr. Chem.* **1976**, *61*, 133 – 181.
[99] R. Bashyam, P. Zelenay, *Nature* **2006**, *443*, 63 – 66.
[100] G. Wu, K. L. More, C. M. Johnston, P. Zelenay, *Science* **2011**, *332*, 443 – 447.
[101] K. Gong, F. Du, Z. Xia, M. Durstock, L. Dai, *Science* **2009**, *323*, 760 – 764.
[102] a) Y. Zhang, K. Fugane, T. Mori, L. Niu, J. Ye, *J. Mater. Chem.* **2012**, *22*, 6575 – 6580; b) L. Qu, Y. Liu, J.-B. Baek, L. Dai, *ACS Nano* **2010**, *4*, 1321 – 1326; c) Z.-H. Sheng, L. Shao, J.-J. Chen, W.-J. Bao, F.-B. Wang, X.-H. Xia, *ACS Nano* **2011**, *5*, 4350 – 4358.
[103] a) Y. Zheng, Y. Jiao, J. Chen, J. Liu, J. Liang, A. Du, W. Zhang, Z. Zhu, S. C. Smith, M. Jaroniec, G. Q. Lu, S. Z. Qiao, *J. Am. Chem. Soc.* **2011**, *133*, 20116 – 20119; b) Y. Sun, C. Li, G. Shi, *J. Mater. Chem.* **2012**, *22*, 12810 – 12816; c) J. Liang, Y. Zheng, J. Chen, J. Liu, D. Hulicova-Jurcakova, M. Jaroniec, S. Z. Qiao, *Angew. Chem.* **2012**, *124*, 3958 – 3962; *Angew. Chem. Int. Ed.* **2012**, *51*, 3892 – 3896; d) S. Yang, X. Feng, X. Wang, K. Mullen, *Angew. Chem.* **2011**, *123*, 5451 – 5455; *Angew. Chem. Int. Ed.* **2011**, *50*, 5339 – 5343.
[104] S. Shanmugam, T. Osaka, *Chem. Commun.* **2011**, *47*, 4463 – 4465.
[105] T. Chen, Z. Cai, Z. Yang, L. Li, X. Sun, T. Huang, A. Yu, H. G. Kia, H. Peng, *Adv. Mater.* **2011**, *23*, 4620 – 4625.
[106] Z. Yao, H. Nie, Z. Yang, X. Zhou, Z. Liu, S. Huang, *Chem. Commun.* **2012**, *48*, 1027 – 1029.
[107] a) S. Yang, L. Zhi, K. Tang, X. Feng, J. Maier, K. Müllen, *Adv. Funct. Mater.* **2012**, *22*, 3634 – 3640; b) Z. Yang, Z. Yao, G. Li, G. Fang, H. Nie, Z. Liu, X. Zhou, X. Chen, S. Huang, *ACS Nano* **2012**, *6*, 205 – 211.
[108] Z.-W. Liu, F. Peng, H.-J. Wang, H. Yu, W.-X. Zheng, J. Yang, *Angew. Chem.* **2011**, *123*, 3315 – 3319; *Angew. Chem. Int. Ed.* **2011**, *50*, 3257 – 3261.
[109] L. Yang, S. Jiang, Y. Zhao, L. Zhu, S. Chen, X. Wang, Q. Wu, J. Ma, Y. Ma, Z. Hu, *Angew. Chem.* **2011**, *123*, 7270 – 7273; *Angew. Chem. Int. Ed.* **2011**, *50*, 7132 – 7135.
[110] a) S. Wang, L. Zhang, Z. Xia, A. Roy, D. W. Chang, J.-B. Baek, L. Dai, *Angew. Chem.* **2012**, *124*, 4285 – 4288; *Angew. Chem. Int. Ed.* **2012**, *51*, 4209 – 4212; b) S. Wang, E. Iyyamperumal, A. Roy, Y. Xue, D. Yu, L. Dai, *Angew. Chem.* **2011**, *123*, 11960 – 11964; *Angew. Chem. Int. Ed.* **2011**, *50*, 11756 – 11760.
[111] Y. Liang, Y. Li, H. Wang, J. Zhou, J. Wang, T. Regier, H. Dai, *Nat. Mater.* **2011**, *10*, 780 – 786.
[112] Y. Liang, H. Wang, J. Zhou, Y. Li, J. Wang, T. Regier, H. Dai, *J. Am. Chem. Soc.* **2012**, *134*, 3517 – 3523.
[113] H. Wang, Y. Liang, Y. Li, H. Dai, *Angew. Chem.* **2011**, *123*, 11161 – 11164; *Angew. Chem. Int. Ed.* **2011**, *50*, 10969 – 10972.
[114] Y. Tan, C. Xu, G. Chen, X. Fang, N. Zheng, Q. Xie, *Adv. Funct. Mater.* **2012**, *22*, 4584 – 4591.
[115] X.-Y. Yan, X.-L. Tong, Y.-F. Zhang, X.-D. Han, Y.-Y. Wang, G.-Q. Jin, Y. Qin, X.-Y. Guo, *Chem. Commun.* **2012**, *48*, 1892 – 1894.
[116] Y. Li, Y. Zhao, H. Cheng, Y. Hu, G. Shi, L. Dai, L. Qu, *J. Am. Chem. Soc.* **2012**, *134*, 15 – 18.
[117] S. Guo, S. Zhang, L. Wu, S. Sun, *Angew. Chem.* **2012**, *124*, 11940 – 11943; *Angew. Chem. Int. Ed.* **2012**, *51*, 11770 – 11773.
[118] Y. Li, W. Zhou, H. Wang, L. Xie, Y. Liang, F. Wei, J.-C. Idrobo, S. J. Pennycook, H. Dai, *Nat. Nanotechnol.* **2012**, *7*, 394 – 400.